Journal Pre-proof

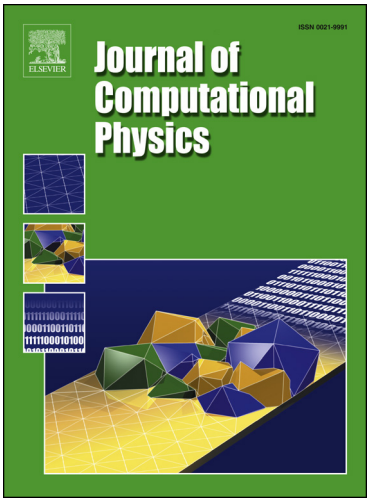

High-order adapter schemes for cell-centered finite difference method

Fei Liao, Guowei He

PII: S0021-9991(19)30795-8
DOI: https://doi.org/10.1016/j.jcp.2019.109090
Reference: YJCPH 109090

To appear in: *Journal of Computational Physics*

Received date: 5 November 2018
Revised date: 29 October 2019
Accepted date: 30 October 2019

Please cite this article as: F. Liao, G. He, High-order adapter schemes for cell-centered finite difference method, *J. Comput. Phys.* (2019), 109090, doi: https://doi.org/10.1016/j.jcp.2019.109090.

High-Order Adapter Schemes for Cell-Centered Finite Difference Method

Fei Liao*, Guowei He†

State Key Laboratory of Nonlinear Mechanics, Institute of Mechanics, Chinese Academy of Science, Beijing 100190

November 6, 2019

Abstract

The present paper proposes that reconstruction scheme and interpolation scheme can be converted into each other through two series of adapter schemes, which include reconstruction-to-interpolation (RI) adapter schemes and interpolation-to-reconstruction (IR) adapter schemes. For the high-order spatial discretization of the compressible Navier-Stokes equations, the RI adapter schemes can be used to derive interpolation schemes for the interpolation-based cell-centered finite difference method from the available optimized reconstruction schemes. The main advantage of the interpolation-based cell-centered finite difference method is the capability to realize high-order discretization on curvilinear grids with both shock-capturing capability and satisfaction of the geometric conservation law. In the present paper, we first derive the IR adapter schemes by comparing the difference schemes with their strong conservative forms. We then develop the corresponding RI adapter schemes by inversing the IR adapter schemes. Thereafter, the applications to the one-dimensional linear wave equation and the one-dimensional inviscid Burgers' equation have been briefly discussed. Finally, to demonstrate the application to three-dimensional Navier-Stokes equations, three highly optimized nonlinear reconstruction schemes are adapted into the corresponding interpolation ones through RI adapter schemes, which include WENO-CU6, WGVC-WENO7 and OMP6 schemes. The new interpolation schemes from adapters are compared with their original reconstruction ones through several benchmark cases. No noticeable robustness loss or accuracy loss has been found in these cases, indicating the effectiveness of the adapter schemes. No obvious increase in time cost has been observed, indicating the efficiency of the adapter schemes.

Keywords: high-order scheme; geometric conservation law; finite difference method; adapter scheme; multiblock grids;

1 Introduction

In computational fluid dynamics (CFD), high-order high-resolution spatial discretization has been studied extensively. Compared with the high-order methods on unstructured mesh, such as discontinuous Galerkin [1] and flux reconstruction [2], the finite difference methods on structured grids, which include the dispersion-relation-preserving (DRP) scheme [3], weighted essentially non-oscillatory (WENO) scheme [4] and weighted compact nonlinear scheme (WCNS) [5] etc., are computationally efficient due to multi-dimensional decomposition of discretization in each individual direction, leading to their wide applications in turbulent flows and aeroacoustics.

In wave propagation problem for aeroacoustics, Tam and Webb [3] developed the DRP scheme for linearized Euler equations. This DRP scheme is a 4th-order linear node-to-node difference scheme optimized for dispersion property on a 6-point stencil. The DRP scheme is usually used in the simulations of low-speed flows.

*Postdoc, 89f.liao@gmail.com

†Corresponding Author, Professor, hgw@lnm.imech.ac.cn

In discontinuous flows, Jiang and Shu [4] successfully developed WENO-JS scheme for both finite difference methods and finite volume methods. The key idea of WENO scheme is to introduce multi-stencil weighting technique to recover optimal order in smooth flow regions on the basis of the essentially non-oscillatory (ENO) scheme. Based on WENO-JS scheme, many variants have been developed, such as the Mapped WENO from Henrick et al. [6], WENO-Z from Borges et al. [7] and WENO-CU6 [8] from Hu and Adams. Based on an early discussion [9] about the freestream preservation of WENO and WCNS on non-Cartesian grids, the alternative flux formulation of finite difference WENO from Jiang et al. [10] and the Freestream Preserving WENO (PFWENO) from Nonomura et al. [11] have been proposed to reduce the geometric errors on highly curvilinear grids and randomized grids to further improve the robustness on non-Cartesian grids.

The WCNS method proposed by Deng and Mao [5] is another promising shock-capturing scheme based on multi-stencil weighting technique. An important advantage or feature of the WCNS method is that the variable interpolation is performed on the primitive/conservative/characteristic variables from the solution points to the flux points. Therefore, flux difference splitting schemes, such as Roe scheme, which has reasonable dissipation, are applicable in WCNS. After the first discussion [9] on the freestream preservation of WCNS, a symmetrical conservative metric method (SCMM) was later proposed by Deng et al. [12] for the WCNS to satisfy the geometric conservation law (GCL) on multiblock curvilinear grids, which greatly increases its robustness in three-dimensional practical simulations. Another advantage of the WCNS method was found by Nonomura et al. [13] that the high-order WCNS is very suitable for the simulation of multi-component flows when the interpolation of primitive variables and the quasi-conservative form of mass fraction equations are adopted.

The cell-centered finite difference method (CCFDM) [14] is the cell-centered version of the interpolation-based WCNS method on multiblock curvilinear grids. In CCFDM, solution points are placed at high-order cell centers while flux points are located at high-order face centers, which totally eliminates the overlapped solution points at multiblock interfaces, leading to better conservation in numeric. To satisfy GCL on curvilinear grids, the cell-centered symmetrical metric method (CCSCMM) has been designed for the geometric discretization for CCFDM. The technical roadmap of current research is illustrated in Fig.1.

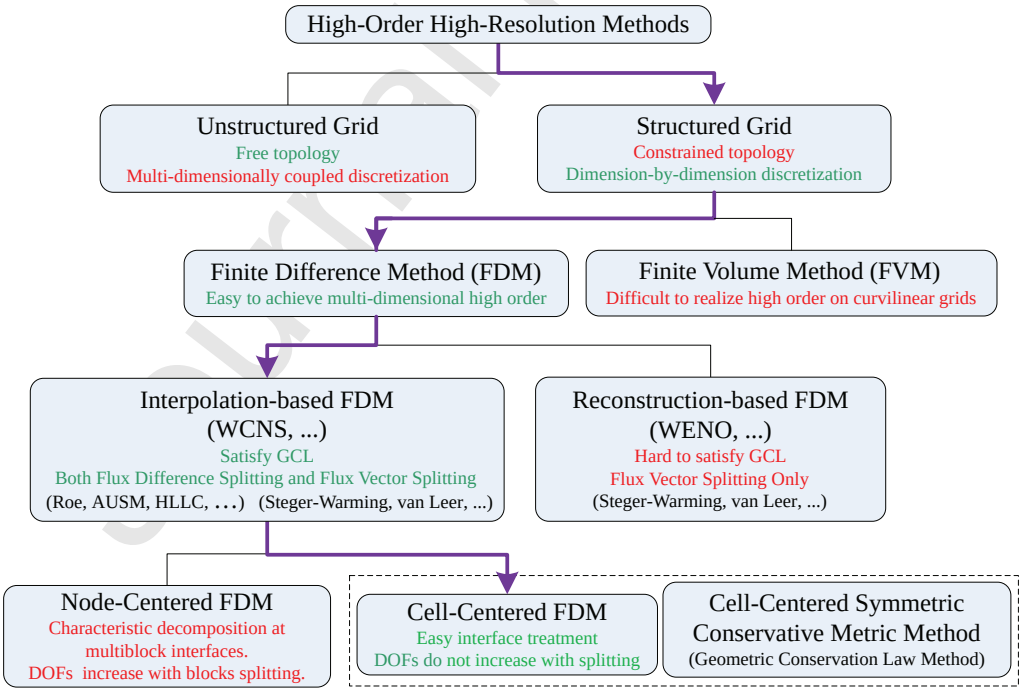

Figure 1: Technical Roadmap of Current Research

The reconstruction schemes are more widely used than the interpolation schemes in both finite volume method and finite difference method. However, deriving optimized high-order high-resolution nonlinear

scheme is usually time consuming and inefficient due to the difficulty in the balance between robustness and accuracy. To obtain optimized high-order high-resolution interpolation schemes for CCFDM, this paper proposes a series of reconstruction-to-interpolation (RI) linear adapter schemes which are able to convert those highly optimized nonlinear reconstruction schemes into the corresponding interpolation ones. This approach is different from the previous one where optimized interpolation schemes are directly derived. With the proposed adapter schemes, the accuracy and robustness of the nonlinear reconstruction schemes can be mainly preserved.

This paper is arranged as follows. In section 2, governing equations in curvilinear coordinates are derived with a brief discussion on GCL. In section 3.1 and 3.2, CCFDM and CCSCMM are introduced as discretization methods for flow variables and geometric variables, respectively. In section 3.3 and 3.4, two series of adapter schemes, IR adapter schemes and RI adapter schemes, are derived and discussed. In section 3.5, the RI adapter schemes are applied to CCFDM to convert three well-optimized reconstruction schemes, which are WENO-CU6, WGVC-WENO7 and OMP6 schemes, into corresponding interpolation ones. In section 4, the methodologies are validated with several benchmark cases, which include 3D freestream preservation, 1D Shu-Osher problem, 1D shock tube problem, 2D isentropic vortex problem, 2D shock wave impingement on spatially evolving mixing layer and 2D shock vortex interaction. Finally, this paper is concluded in section 5.

2 Governing Equations

In the Cartesian coordinates, the non-dimensional compressible Navier-Stokes equations can be written as

$$\frac{\partial Q}{\partial t}+\frac{\partial E}{\partial x}+\frac{\partial F}{\partial y}+\frac{\partial G}{\partial z}=\frac{M}{Re}\left(\frac{\partial E_v}{\partial x}+\frac{\partial F_v}{\partial y}+\frac{\partial G_v}{\partial z}\right) \tag{1}$$

where

$$Q=\begin{pmatrix}\rho\\ \rho u\\ \rho v\\ \rho w\\ \rho e\end{pmatrix},\quad E=\begin{pmatrix}\rho u\\ \rho u^2+p\\ \rho vu\\ \rho wu\\ (\rho e+p)u\end{pmatrix},\quad F=\begin{pmatrix}\rho v\\ \rho uv\\ \rho v^2+p\\ \rho wv\\ (\rho e+p)v\end{pmatrix},\quad G=\begin{pmatrix}\rho w\\ \rho uw\\ \rho vw\\ \rho w^2+p\\ (\rho e+p)w\end{pmatrix}, \tag{2}$$

$$E_v=\begin{pmatrix}0\\ \tau_{11}\\ \tau_{12}\\ \tau_{13}\\ \varphi_1\end{pmatrix},\quad F_v=\begin{pmatrix}0\\ \tau_{21}\\ \tau_{22}\\ \tau_{23}\\ \varphi_2\end{pmatrix},\quad G_v=\begin{pmatrix}0\\ \tau_{31}\\ \tau_{32}\\ \tau_{33}\\ \varphi_3\end{pmatrix}, \tag{3}$$

and

$$\rho e=\frac{p}{\gamma-1}+\frac{1}{2}\rho u_i^2, \tag{4}$$

in which u_i $(i=1,2,3)$ stand for u, v and w. And the pressure p can be calculated by the following non-dimensional equation according to the ideal gas equation of state

$$p=\frac{\rho T}{\gamma}. \tag{5}$$

The viscous stress and heat flux related terms have the following form

$$\tau_{ij}=\mu\left(\frac{\partial u_i}{\partial x_j}+\frac{\partial u_j}{\partial x_i}\right)-\frac{2}{3}\mu\delta_{ij}\frac{\partial u_k}{\partial x_k}, \tag{6}$$

$$\varphi_i=u_j\tau_{ij}+k\frac{\partial T}{\partial x_i},\quad k=\frac{C_p\mu}{P_r}. \tag{7}$$

where x_i $(i=1,2,3)$ stand for x, y and z.

It should be stated that the above equations are non-dimensionalized by introducing the following dimensional freestream parameters as reference: freestream sound of speed c^*_∞ for velocity, freestream ρ^*_∞ for density, freestream T^*_∞ for temperature, freestream μ^*_∞ for dynamic viscosity, freestream κ^*_∞ for heat conductivity, $(c^*_\infty)^2$ for energy, $\rho^*_\infty(c^*_\infty)^2$ for pressure, and L^*/c^*_∞ for time, where L^* is the length used for grid non-dimensionalization. To be specific, they are

$$
\begin{aligned}
&M = \frac{u^*_\infty}{c^*_\infty}, \quad Re = \frac{\rho^*_\infty u^*_\infty L*}{\mu^*_\infty}, \quad \frac{M}{Re} = \left(\frac{\rho^*_\infty c^*_\infty L*}{\mu^*_\infty}\right)^{-1}, \\
&\rho = \frac{\rho^*}{\rho^*_\infty}, \quad p = \frac{p^*}{\rho^*_\infty (c^*_\infty)^2}, \quad T = \frac{T^*}{T^*_\infty}, \quad e = \frac{e^*}{(c^*_\infty)^2}, \\
&(u, v, w, c) = \frac{(u^*, v^*, w^*, c^*)}{c^*_\infty}, \quad (x, y, z) = \frac{(x^*, y^*, z^*)}{L^*}, \quad t = \frac{t^* c^*_\infty}{L^*},
\end{aligned}
\tag{8}
$$

where the superscript* refers to dimensional variables. And the obtained non-dimensional freestream parameters are

$$
\rho_\infty = 1, \quad p_\infty = \frac{1}{\gamma}, \quad T_\infty = 1, \quad e_\infty = \frac{1}{\gamma(\gamma-1)} + \frac{M^2}{2}, \quad (u, v, w, c)_\infty = (M, 0, 0, 1). \tag{9}
$$

By introducing coordinate transformation on stationary grids

$$
x = x(\xi, \eta, \zeta), \;\; y = y(\xi, \eta, \zeta), \;\; z = z(\xi, \eta, \zeta), \tag{10}
$$

$$
J = \begin{vmatrix} \dfrac{\partial x}{\partial \xi} & \dfrac{\partial x}{\partial \eta} & \dfrac{\partial x}{\partial \zeta} \\ \dfrac{\partial y}{\partial \xi} & \dfrac{\partial y}{\partial \eta} & \dfrac{\partial y}{\partial \zeta} \\ \dfrac{\partial z}{\partial \xi} & \dfrac{\partial z}{\partial \eta} & \dfrac{\partial z}{\partial \zeta} \end{vmatrix}, \tag{11}
$$

the inviscid flux terms in Eqs. (1) can be expressed as

$$
\begin{aligned}
\frac{\partial E}{\partial x} + \frac{\partial F}{\partial y} + \frac{\partial G}{\partial z} &= \frac{\partial E}{\partial \xi_i}\frac{\partial \xi_i}{\partial x} + \frac{\partial F}{\partial \xi_i}\frac{\partial \xi_i}{\partial y} + \frac{\partial G}{\partial \xi_i}\frac{\partial \xi_i}{\partial z} \\
&= \frac{1}{J}\frac{\partial E}{\partial \xi_i} J \frac{\partial \xi_i}{\partial x} + \frac{1}{J}\frac{\partial F}{\partial \xi_i} J \frac{\partial \xi_i}{\partial y} + \frac{1}{J}\frac{\partial G}{\partial \xi_i} J \frac{\partial \xi_i}{\partial z} \\
&= \frac{1}{J}\frac{\partial}{\partial \xi_i}\left(EJ\frac{\partial \xi_i}{\partial x}\right) - \frac{1}{J}E\underbrace{\frac{\partial}{\partial \xi_i}\left(J\frac{\partial \xi_i}{\partial x}\right)}_{I_x} \\
&\quad + \frac{1}{J}\frac{\partial}{\partial \xi_i}\left(FJ\frac{\partial \xi_i}{\partial y}\right) - \frac{1}{J}F\underbrace{\frac{\partial}{\partial \xi_i}\left(J\frac{\partial \xi_i}{\partial y}\right)}_{I_y} \\
&\quad + \frac{1}{J}\frac{\partial}{\partial \xi_i}\left(GJ\frac{\partial \xi_i}{\partial z}\right) - \frac{1}{J}G\underbrace{\frac{\partial}{\partial \xi_i}\left(J\frac{\partial \xi_i}{\partial z}\right)}_{I_z} \\
&= \frac{1}{J}\frac{\partial}{\partial \xi_i}\left(EJ\frac{\partial \xi_i}{\partial x}\right) + \frac{1}{J}\frac{\partial}{\partial \xi_i}\left(FJ\frac{\partial \xi_i}{\partial y}\right) + \frac{1}{J}\frac{\partial}{\partial \xi_i}\left(GJ\frac{\partial \xi_i}{\partial z}\right) \\
&= \frac{1}{J}\left(\frac{\partial \hat{E}}{\partial \xi} + \frac{\partial \hat{F}}{\partial \eta} + \frac{\partial \hat{G}}{\partial \zeta}\right)
\end{aligned}
\tag{12}
$$

Equation for viscous terms E_v, F_v and G_v can be obtained in the very same way.

It should be noticed that in Eqs. (12), several conditions should be satisfied. The third line in Eqs. (12) requires the satisfaction of the following equation in discretized form

$$(f \cdot g)' = f' \cdot g + f \cdot g', \tag{13}$$

which will not be discussed in this paper. And the sixth line in Eqs. (12) requires the following conditions to be satisfied in numeric

$$\begin{aligned} I_x &= (J\xi_x)_\xi + (J\eta_x)_\eta + (J\zeta_x)_\zeta = 0, \\ I_y &= (J\xi_y)_\xi + (J\eta_y)_\eta + (J\zeta_y)_\zeta = 0, \\ I_z &= (J\xi_z)_\xi + (J\eta_z)_\eta + (J\zeta_z)_\zeta = 0, \end{aligned} \tag{14}$$

which represent the surface conservation law (SCL) of the geometric conservation law (GCL).

It should be clarified that in Eqs. (12), the notation ξ_i $(i = 1, 2, 3)$ stand for ξ, η and ζ. And the notation ξ_x in Eqs. (14) stands for $\partial\xi/\partial x$.

Finally, the Navier-Stokes equations in curvilinear coordinates can be rewritten as

$$\frac{\partial \hat{Q}}{\partial t} + \frac{\partial \hat{E}}{\partial \xi} + \frac{\partial \hat{F}}{\partial \eta} + \frac{\partial \hat{G}}{\partial \zeta} = \frac{M}{Re}\left(\frac{\partial \hat{E}_v}{\partial \xi} + \frac{\partial \hat{F}_v}{\partial \eta} + \frac{\partial \hat{G}_v}{\partial \zeta}\right) \tag{15}$$

where

$$\begin{aligned} \hat{Q} &= JQ, \\ \hat{E} &= J\xi_x E + J\xi_y F + J\xi_z G, \\ \hat{F} &= J\eta_x E + J\eta_y F + J\eta_z G, \\ \hat{G} &= J\zeta_x E + J\zeta_y F + J\zeta_z G, \\ \hat{E}_v &= J\xi_x E_v + J\xi_y F_v + J\xi_z G_v, \\ \hat{F}_v &= J\eta_x E_v + J\eta_y F_v + J\eta_z G_v, \\ \hat{G}_v &= J\zeta_x E_v + J\zeta_y F_v + J\zeta_z G_v. \end{aligned} \tag{16}$$

3 Numerical Methods

This paper focused on the cell-centered discretization method. Before further introduction, the notations for node, edge, face and cell should be clarified. In the following sub-sections, (i, j, k) and $(i \pm 1/2, j \pm 1/2, k \pm 1/2)$ represent the cell centers and the grid nodes, respectively. And the notations $(i \pm 1/2, j, k)$, $(i, j \pm 1/2, k)$ and $(i, j, k \pm 1/2)$ stand for the face centers in each of the ξ, η and ζ directions. After grid generation, only the coordinates at grid nodes are known at first.

The solution points and flux points are located at cell centers and face centers, respectively. In the following part of this paper with one-dimensional demonstration, the cell centers are usually represented with subscripts $i-1$, i, $i+1$ etc., and the face centers are always denoted by the subscripts $i-1/2$, $i+1/2$ etc. And all the variables computed at face centers will have truncation error. In the rest of this paper, the truncation error at face centers are neglected to keep simple and clear.

3.1 Cell-Centered Finite Difference Method

In this section, the discretization for flow variables is introduced and discussed. The main problem is to obtain the spatial terms $\hat{E}_\xi$, $\hat{F}_\eta$ and $\hat{G}_\zeta$ for Eqs. (15). In the rest of this section, term $\hat{E}_\xi$ is focused as illustration.

The original WCNS-E-5 proposed by Deng [5] use the following 6th-order difference scheme

$$\delta^\xi \hat{E}_i = \frac{75}{64}(\hat{E}_{i+1/2} - \hat{E}_{i-1/2}) - \frac{25}{384}(\hat{E}_{i+3/2} - \hat{E}_{i-3/2}) + \frac{3}{640}(\hat{E}_{i+5/2} - \hat{E}_{i-5/2}). \tag{17}$$

To achieve robust solution in the flows with strong shocks, Deng et al. [15] take the flux at cell centers into the difference procedure, and obtain the following 6th-order difference scheme

$$\delta^{\xi}\hat{E}_i = \frac{64}{45}(\hat{E}_{i+1/2} - \hat{E}_{i-1/2}) - \frac{2}{9}(\hat{E}_{i+1} - \hat{E}_{i-1}) + \frac{1}{180}(\hat{E}_{i+2} - \hat{E}_{i-2}). \tag{18}$$

Later, Nonomura and Fujii [16] proposed the following scheme to avoid undershoot or overshoot in strong discontinuities

$$\delta^{\xi}\hat{E}_i = \frac{3}{2}(\hat{E}_{i+1/2} - \hat{E}_{i-1/2}) - \frac{3}{10}(\hat{E}_{i+1} - \hat{E}_{i-1}) + \frac{1}{30}(\hat{E}_{i+3/2} - \hat{E}_{i-3/2}). \tag{19}$$

Eqs. (17) is called face-to-cell (F-to-C) difference scheme in this paper. And both Eqs. (18) and (19) are called face-and-cell-to-cell (FC-to-C) difference schemes in this paper. To be specific, Eqs. (18) from Deng [15] is called FC-to-C-D in this paper, and the scheme indicated by Eqs. (19) from Nonomura [16] is denoted as FC-to-C-N in this paper.

As it is described before, the solution points and flux points are located at cell centers and face centers, respectively. In F-to-C difference scheme, only face centers are adopted to obtain the derivative. Any flux-differencing-splitting (FDS) scheme can be used for the face flux, such as Roe scheme [17]:

$$\hat{E}_{i+1/2} = Roe(Q^L_{i+1/2}, Q^R_{i+1/2}, J\xi_x, J\xi_y, J\xi_z), \tag{20}$$

where Q^L and Q^R are interpolated to the left and right side of the face $i+1/2$. In FC-to-C schemes, the additional cell flux can be directly calculated by

$$\hat{E}_i = Flux(Q_i, J\xi_x, J\xi_y, J\xi_z) = \begin{pmatrix} \rho U \\ \rho u U + pJ\xi_x \\ \rho v U + pJ\xi_y \\ \rho w U + pJ\xi_z \\ (\rho e + p)U \end{pmatrix}_i, \tag{21}$$

where $U = uJ\xi_x + vJ\xi_y + wJ\xi_z$.

According to previous research [16] [18], two key points can be observed. First, the difference scheme has close relation to the robustness of the whole method but has minor effects on the analytical resolution of the whole method. Second, the performance of the whole method is mainly determined by the interpolation scheme, which will be focused on in the following sections.

The method described in this section is named as the cell-centered finite difference method (CCFDM) in [14].

3.2 Cell-Centered Symmetrical Conservative Metric Method

In this section, the discretization for geometric variables is introduced, which indicates the x,y,z related metrics and Jacobians. Many researches [12][19][20] have been focused on the geometric conservation law (GCL).

It has been shown in the previous section that the surface conservation law (SCL) should be satisfied when Eqs.(15) are used. To satisfy SCL, the following equations [21][22] are adopted

$$\begin{aligned} J\xi_x &= \frac{(J\xi_x)^{S1} + (J\xi_x)^{S2}}{2}, \quad J\xi_y = \frac{(J\xi_y)^{S1} + (J\xi_y)^{S2}}{2}, \quad J\xi_z = \frac{(J\xi_z)^{S1} + (J\xi_z)^{S2}}{2}, \\ J\eta_x &= \frac{(J\eta_x)^{S1} + (J\eta_x)^{S2}}{2}, \quad J\eta_y = \frac{(J\eta_y)^{S1} + (J\eta_y)^{S2}}{2}, \quad J\eta_z = \frac{(J\eta_z)^{S1} + (J\eta_z)^{S2}}{2}, \\ J\zeta_x &= \frac{(J\zeta_x)^{S1} + (J\zeta_x)^{S2}}{2}, \quad J\zeta_y = \frac{(J\zeta_y)^{S1} + (J\zeta_y)^{S2}}{2}, \quad J\zeta_z = \frac{(J\zeta_z)^{S1} + (J\zeta_z)^{S2}}{2}, \end{aligned} \tag{22}$$

where

$$\begin{aligned} (J\xi_x)^{S1} &= (y_\eta z)_\zeta - (y_\zeta z)_\eta, \quad (J\xi_y)^{S1} = (z_\eta x)_\zeta - (z_\zeta x)_\eta, \quad (J\xi_z)^{S1} = (x_\eta y)_\zeta - (x_\zeta y)_\eta, \\ (J\eta_x)^{S1} &= (y_\zeta z)_\xi - (y_\xi z)_\zeta, \quad (J\eta_y)^{S1} = (z_\zeta x)_\xi - (z_\xi x)_\zeta, \quad (J\eta_z)^{S1} = (x_\zeta y)_\xi - (x_\xi y)_\zeta, \\ (J\zeta_x)^{S1} &= (y_\xi z)_\eta - (y_\eta z)_\xi, \quad (J\zeta_y)^{S1} = (z_\xi x)_\eta - (z_\eta x)_\xi, \quad (J\zeta_z)^{S1} = (x_\xi y)_\eta - (x_\eta y)_\xi, \end{aligned} \tag{23}$$

and

$$
\begin{aligned}
&(J\xi_x)^{S2} = (z_\zeta y)_\eta - (z_\eta y)_\zeta, \quad (J\xi_y)^{S2} = (x_\zeta z)_\eta - (x_\eta z)_\zeta, \quad (J\xi_z)^{S2} = (y_\zeta x)_\eta - (y_\eta x)_\zeta, \\
&(J\eta_x)^{S2} = (z_\xi y)_\zeta - (z_\zeta y)_\xi, \quad (J\eta_y)^{S2} = (x_\xi z)_\zeta - (x_\zeta z)_\xi, \quad (J\eta_z)^{S2} = (y_\xi x)_\zeta - (y_\zeta x)_\xi, \\
&(J\zeta_x)^{S2} = (z_\eta y)_\xi - (z_\xi y)_\eta, \quad (J\zeta_y)^{S2} = (x_\eta z)_\xi - (x_\xi z)_\eta, \quad (J\zeta_z)^{S2} = (y_\eta x)_\xi - (y_\xi x)_\eta.
\end{aligned}
\tag{24}
$$

The above equations originate from the node-centered symmetrical conservative metric method (SCMM) in previous research [12] [20]. Then, SCMM is further extended to the cell-centered method using the following equations

$$
(J\xi_x)^{S1} = \underbrace{\delta_2^\zeta(\underset{edge-\eta}{z}\underbrace{\delta_3^\eta \underset{node}{y}}_{edge-\eta})}_{face-\eta\zeta} - \underbrace{\delta_2^\eta(\underset{edge-\zeta}{z}\underbrace{\delta_3^\zeta \underset{node}{y}}_{edge-\zeta})}_{face-\eta\zeta},
\tag{25}
$$

$$
\begin{aligned}
J = \frac{1}{3}\{ & \underbrace{\delta_1^\xi[\underset{face-\eta\zeta}{x}\underbrace{(J\xi_x)}_{face-\eta\zeta} + \underset{face-\eta\zeta}{y}\underbrace{(J\xi_y)}_{face-\eta\zeta} + \underset{face-\eta\zeta}{z}\underbrace{(J\xi_z)}_{face-\eta\zeta}]}_{cell-\xi\eta\zeta} \\
& + \underbrace{\delta_1^\eta[\underset{face-\xi\zeta}{x}\underbrace{(J\eta_x)}_{face-\xi\zeta} + \underset{face-\xi\zeta}{y}\underbrace{(J\eta_y)}_{face-\xi\zeta} + \underset{face-\xi\zeta}{z}\underbrace{(J\eta_z)}_{face-\xi\zeta}]}_{cell-\xi\eta\zeta} \\
& + \underbrace{\delta_1^\zeta[\underset{face-\xi\eta}{x}\underbrace{(J\zeta_x)}_{face-\xi\eta} + \underset{face-\xi\eta}{y}\underbrace{(J\zeta_y)}_{face-\xi\eta} + \underset{face-\xi\eta}{z}\underbrace{(J\zeta_z)}_{face-\xi\eta}]}_{cell-\xi\eta\zeta}\}.
\end{aligned}
\tag{26}
$$

where the difference operators are divided into three categories: the node-to-edge difference operator δ_3, the edge-to-face difference operator δ_2 and the face-to-cell difference operator δ_1, representing that the geometric information is gradually transformed from node to edge, from edge to face and from face to cell, respectively.

For arbitrary variable V, the node-to-edge difference operator δ_3 is defined by

$$
\underset{edge-\xi}{V'_\xi} = \delta_3^\xi(\underset{node}{V}), \quad \underset{edge-\eta}{V'_\eta} = \delta_3^\eta(\underset{node}{V}), \quad \underset{edge-\zeta}{V'_\zeta} = \delta_3^\zeta(\underset{node}{V}).
\tag{27}
$$

Similarly, the edge-to-face difference operator δ_2 is defined by

$$
\begin{aligned}
&\underset{face-\xi\eta}{V'_\xi} = \delta_2^\xi(\underset{edge-\eta}{V}), \quad \underset{face-\xi\zeta}{V'_\xi} = \delta_2^\xi(\underset{edge-\zeta}{V}), \quad \underset{face-\eta\zeta}{V'_\eta} = \delta_2^\eta(\underset{edge-\zeta}{V}), \\
&\underset{face-\xi\eta}{V'_\eta} = \delta_2^\eta(\underset{edge-\xi}{V}), \quad \underset{face-\xi\zeta}{V'_\zeta} = \delta_2^\zeta(\underset{edge-\xi}{V}), \quad \underset{face-\eta\zeta}{V'_\zeta} = \delta_2^\zeta(\underset{edge-\eta}{V}).
\end{aligned}
\tag{28}
$$

And the face-to-cell difference operator δ_1 is defined by

$$
\underset{cell-\xi\eta\zeta}{V'_\xi} = \delta_1^\xi(\underset{face-\eta\zeta}{V}), \quad \underset{cell-\xi\eta\zeta}{V'_\eta} = \delta_1^\eta(\underset{face-\xi\zeta}{V}), \quad \underset{cell-\xi\eta\zeta}{V'_\zeta} = \delta_1^\zeta(\underset{face-\xi\eta}{V}).
\tag{29}
$$

To be specific, second-order differencing is demonstrated as illustration

$$
V'_i = V_{i+1/2} - V_{i-1/2}.
\tag{30}
$$

Note that in Eqs.(25) and (26), the coordinates x, y and z are not only needed at node, but also wanted at edge centers and face centers. Thus, a series of linear central schemes are introduced for the interpolation of geometric coordinates.

The node-to-edge linear interpolation operator χ_3 is defined as

$$
\underset{edge-\xi}{V} = \chi_3^\xi(\underset{node}{V}), \quad \underset{edge-\eta}{V} = \chi_3^\eta(\underset{node}{V}), \quad \underset{edge-\zeta}{V} = \chi_3^\zeta(\underset{node}{V}).
\tag{31}
$$

The edge-to-face linear interpolation operator χ_2 is defined as

$$\begin{aligned}
\underset{face-\xi\eta}{V} &= \frac{1}{2}[\chi_2^{\xi}(\underset{edge-\eta}{V}) + \chi_2^{\eta}(\underset{edge-\xi}{V})],\\
\underset{face-\xi\zeta}{V} &= \frac{1}{2}[\chi_2^{\xi}(\underset{edge-\zeta}{V}) + \chi_2^{\zeta}(\underset{edge-\xi}{V})],\\
\underset{face-\eta\zeta}{V} &= \frac{1}{2}[\chi_2^{\eta}(\underset{edge-\zeta}{V}) + \chi_2^{\zeta}(\underset{edge-\eta}{V})].
\end{aligned} \tag{32}$$

And the face-to-cell linear interpolation operator χ_1 is defined as

$$\underset{cell-\xi\eta\zeta}{V} = \frac{1}{3}[\chi_1^{\xi}(\underset{face-\eta\zeta}{V}) + \chi_1^{\eta}(\underset{edge-\xi\zeta}{V}) + \chi_1^{\zeta}(\underset{edge-\xi\eta}{V})]. \tag{33}$$

The second-order scheme is demonstrated as illustration

$$V_i = \frac{1}{2}(V_{i-1/2} + V_{i+1/2}). \tag{34}$$

In this paper, we choose

$$\delta_1^{\xi} = \delta_2^{\xi} = \delta_3^{\xi},\ \ \delta_1^{\eta} = \delta_2^{\eta} = \delta_3^{\eta},\ \ \delta_1^{\zeta} = \delta_2^{\zeta} = \delta_3^{\zeta}, \tag{35}$$

$$\chi_1^{\xi} = \chi_2^{\xi} = \chi_3^{\xi},\ \ \chi_1^{\eta} = \chi_2^{\eta} = \chi_3^{\eta},\ \ \chi_1^{\zeta} = \chi_2^{\zeta} = \chi_3^{\zeta}. \tag{36}$$

The method described in this section is called the cell-centered symmetrical conservative metric method (CCSCMM) in [14].

3.3 Interpolation-to-Reconstruction (IR) Adapter Schemes

To begin with, we focus on the discretization of $\partial u/\partial\xi$ at cell center i, where u is an arbitrary variable.

In the reconstruction-based finite difference method, the derivative $\partial u/\partial\xi$ is obtained by

$$\left(\frac{\partial u}{\partial \xi}\right)_i = \delta^{\xi} u_i = \underbrace{\tilde{u}_{i+1/2} - \tilde{u}_{i-1/2}}_{\text{face: reconstructed}}, \tag{37}$$

where the $\tilde{u}$ is implicitly defined by

$$u(\xi) = \frac{1}{\Delta\xi}\int_{-\frac{\Delta\xi}{2}}^{\frac{\Delta\xi}{2}} \tilde{u}(\xi + s)ds. \tag{38}$$

Arbitrary reconstruction scheme can be applied to obtain $\tilde{u}_{i\pm1/2}$ with the known u_i, u_{i-1}, u_{i+1}, etc. at solution points. The linear part of the WENO scheme [4] is utilized here as demonstration

$$\tilde{u}_{i+1/2}^{L} = \frac{1}{30}u_{i-2} - \frac{13}{60}u_{i-1} + \frac{47}{60}u_i + \frac{9}{20}u_{i+1} - \frac{1}{20}u_{i+2}, \tag{39}$$

where the superscript L indicates the upwind reconstruction to the left side of $i + 1/2$.

While in the interpolation-based finite difference method, the derivative $\partial u/\partial\xi$ is computed by

$$\left(\frac{\partial u}{\partial \xi}\right)_i = \delta^{\xi} u_i = \sum_{l=0}^{Na} a_l \underbrace{(u_{i+l+1/2} - u_{i-l-1/2})}_{\text{face: interpolated}} + \sum_{l=1}^{Nb} b_l \underbrace{(u_{i+l} - u_{i-l})}_{\text{cell: solution points}}, \tag{40}$$

where the $u_{i\pm1}$, $u_{i\pm2}$, $\cdots$ at cell centers are known in the beginning, and the $u_{i\pm1/2}$, $u_{i\pm3/2}$, $\cdots$ at face centers are computed through interpolation schemes. The linear part of the WCNS scheme [5] is used here as demonstration

$$u_{i+1/2}^{L} = \frac{3}{128}u_{i-2} - \frac{20}{128}u_{i-1} + \frac{90}{128}u_i + \frac{60}{128}u_{i+1} - \frac{5}{128}u_{i+2}. \tag{41}$$

The coefficients a_l and b_l for 2nd-order to 10th-order difference schemes by Eq.(40) are listed in Table 1. In Table 1, if all b_l equal to 0, the obtained schemes are called face-to-cell (F-to-C) difference, otherwise they are called face-and-cell-to-cell (FC-to-C) difference in this paper. The FC-to-C-D series are based on the HWCNS from Deng [15], while the FC-to-C-N schemes originate from the WCNS-MND schemes from Nonomura [16]. It can be seen that F-to-C-2, FC-to-C-D2 and FC-to-C-N2 are the same scheme, and FC-to-C-D4 and FC-to-C-N4 are also the same one. It has been shown by Nonomura [16] that FC-to-C schemes are more robust than F-to-C schemes in the problems with strong shocks. And in the consideration of the width of the discretization stencil, which is vital to the construction Jacobian matrix of the implicit time-integration method, the FC-to-C-D schemes have the most compact cell-to-cell stencil. The cell-to-cell stencil is obtained by substituting the cell-to-face interpolation stencil into the face-to-cell/face-and-cell-to-cell difference stencil. Finally, FC-to-C-D schemes are suggested in the present paper.

Table 1: Coefficients for difference schemes for Eq.(40)

Scheme	a_0	a_1	a_2	a_3	a_4	b_1	b_2	b_3	b_4
F-to-C-2	1								
F-to-C-4	$\frac{9}{8}$	$-\frac{1}{24}$							
F-to-C-6	$\frac{75}{64}$	$-\frac{25}{384}$	$\frac{3}{640}$						
F-to-C-8	$\frac{1225}{1024}$	$-\frac{245}{3072}$	$\frac{49}{5120}$	$-\frac{5}{7168}$					
F-to-C-10	$\frac{19845}{16384}$	$-\frac{735}{8192}$	$\frac{567}{40960}$	$-\frac{405}{229376}$	$\frac{35}{294912}$				
FC-to-C-D2	1								
FC-to-C-D4	$\frac{4}{3}$					$-\frac{1}{6}$			
FC-to-C-D6	$\frac{64}{45}$					$-\frac{2}{9}$	$\frac{1}{180}$		
FC-to-C-D8	$\frac{256}{175}$					$-\frac{1}{4}$	$\frac{1}{100}$	$-\frac{1}{2100}$	
FC-to-C-D10	$\frac{16384}{11025}$					$-\frac{4}{15}$	$\frac{1}{75}$	$-\frac{4}{3675}$	$\frac{1}{17640}$
FC-to-C-N2	1								
FC-to-C-N4	$\frac{4}{3}$					$-\frac{1}{6}$			
FC-to-C-N6	$\frac{3}{2}$	$\frac{1}{30}$				$-\frac{3}{10}$			
FC-to-C-N8	$\frac{8}{5}$	$\frac{8}{105}$				$-\frac{2}{5}$	$-\frac{1}{140}$		
FC-to-C-N10	$\frac{5}{3}$	$\frac{5}{42}$	$\frac{1}{630}$			$-\frac{10}{21}$	$-\frac{5}{252}$		

By comparing the right sides of Eq.(37) and Eq.(40), we could obtain the following relations between the reconstructed $\tilde{u}_{i+1/2}$ and the interpolated $u_{i+1/2}$:

$$\underbrace{\tilde{u}_{i+1/2}}_{\text{face: reconstructed}} = c_0 \underbrace{u_{i+1/2}}_{\text{face: interpolated}} + \sum_{l=1}^{Nc} c_l \underbrace{\left(u_{i+1/2+l} + u_{i+1/2-l}\right)}_{\text{face: interpolated}} + \sum_{l=1}^{Nd} d_l \underbrace{\left(u_{i+l} + u_{i-l+1}\right)}_{\text{cell: solution points}}, \tag{42}$$

which represents the interpolation-to-reconstruction (IR) adapter schemes in the present paper. The coefficients c_l and d_l for different orders are listed in Table 2. Substituting Eq.(42) into Eq.(37) will recover Eq.(40).

It can be seen that the interpolated face value $u_{i+1/2}$ could be converted into the reconstructed face value $\tilde{u}_{i+1/2}$ using Eqs. (42). Thus, the combination of an interpolation scheme and Eqs. (42) can be regarded as a reconstruction scheme. This is the reason why Eqs. (42) is called IR adapter scheme in this paper.

3.4 Reconstruction-to-Interpolation (RI) Adapter Schemes

In the present research, the reconstruction schemes are available but the interpolation schemes are in need. By letting the interpolated face values on the left side and the reconstructed face values on the right side

Table 2: Coefficients for interpolation-to-reconstruction (IR) adapter schemes for Eq.(42)

Scheme	c_0	c_1	c_2	c_3	c_4	d_1	d_2	d_3	d_4
IR-2	1								
IR-4	$\frac{13}{12}$	$-\frac{1}{24}$							
IR-6	$\frac{1067}{960}$	$-\frac{29}{480}$	$\frac{3}{640}$						
IR-8	$\frac{30251}{26880}$	$-\frac{7621}{107520}$	$\frac{159}{17920}$	$-\frac{5}{7168}$					
IR-10	$\frac{5851067}{5160960}$	$-\frac{100027}{1290240}$	$\frac{31471}{2580480}$	$-\frac{425}{258048}$	$\frac{35}{294912}$				
IR-D2	1								
IR-D4	$\frac{4}{3}$					$-\frac{1}{6}$			
IR-D6	$\frac{64}{45}$					$-\frac{13}{60}$	$\frac{1}{180}$		
IR-D8	$\frac{256}{175}$					$-\frac{101}{420}$	$\frac{1}{105}$	$-\frac{1}{2100}$	
IR-D10	$\frac{16384}{11025}$					$-\frac{641}{2520}$	$\frac{31}{2520}$	$-\frac{13}{12600}$	$\frac{1}{17640}$
IR-N2	1								
IR-N4	$\frac{4}{3}$					$-\frac{1}{6}$			
IR-N6	$\frac{23}{15}$	$\frac{1}{30}$				$-\frac{3}{10}$			
IR-N8	$\frac{176}{105}$	$\frac{8}{105}$				$-\frac{57}{140}$	$-\frac{1}{140}$		
IR-N10	$\frac{563}{315}$	$\frac{38}{315}$	$\frac{1}{630}$			$-\frac{125}{252}$	$-\frac{5}{252}$		

of Eqs. (42), we could obtain another series of adapter schemes

$$\underbrace{u_{i+1/2}}_{\text{face: interpolated}} + \sum_{l=1}^{Nh} h_l \underbrace{\left(u_{i+1/2+l} + u_{i+1/2-l}\right)}_{\text{face: interpolated}} = r_0 \underbrace{\tilde{u}_{i+1/2}}_{\text{face: reconstructed}} + \sum_{l=1}^{Nr} r_l \underbrace{\left(u_{i+l} + u_{i-l+1}\right)}_{\text{cell: solution points}}, \tag{43}$$

where the coefficients h_l and r_l can be found in Table 3.

These schemes, indicated by Eqs.(43) and Table 3, are called reconstruction-to-interpolation (RI) adapter schemes in this paper. And it is obvious that when all h_l become zero, Eqs. (43) will be explicit. According to Table 3, it can be seen that the RI schemes originating from F-to-C and FC-to-C-N are implicit and the schemes derived from FC-to-C-D are explicit. Besides, RI-D schemes have the simplicity in boundary treatment, ghost cells of solution points might work. While the RI schemes derived from F-to-C and FC-to-C-N need ghost face of flux points at boundaries, which adds complexity to the application. Thus, only RI-D schemes are focused in the rest of this paper.

3.5 Application to 1D Linear Wave Equation

The one-dimensional (1D) linear wave equation has the following form

$$\frac{\partial u}{\partial t} + \frac{\partial f(u)}{\partial x} = 0, \tag{44}$$

where $f = cu$, and $c > 0$ is constant. The above equation can be discretized as

$$\frac{\partial u}{\partial t} = -\frac{\partial f}{\partial x} = -\frac{1}{\Delta x}\frac{\partial f}{\partial \xi}, \tag{45}$$

where $\partial f/\partial \xi$ is computed by Eq.(40). Here we use FC-to-C-D6 for example

$$\frac{\partial f}{\partial \xi} = \frac{64}{45}\left(f_{i+1/2} - f_{i-1/2}\right) - \frac{2}{9}\left(f_{i+1} - f_{i-1}\right) + \frac{1}{180}\left(f_{i+2} - f_{i-2}\right), \tag{46}$$

Table 3: Coefficients for reconstruction-to-interpolation (RI) adapter schemes for Eq.(43)

Scheme	h_1	h_2	h_3	h_4	r_0	r_1	r_2	r_3	r_4
RI-2					1				
RI-4	$-\frac{1}{26}$				$\frac{12}{13}$				
RI-6	$-\frac{58}{1067}$	$\frac{9}{2134}$			$\frac{960}{1067}$				
RI-8	$-\frac{7621}{121004}$	$\frac{477}{60502}$	$-\frac{75}{121004}$		$\frac{26880}{30251}$				
RI-10	$-\frac{400108}{5851067}$	$\frac{62942}{5851067}$	$-\frac{8500}{5851067}$	$\frac{1225}{11702134}$	$\frac{5160960}{5851067}$				
RI-D2					1				
RI-D4					$\frac{3}{4}$	$\frac{1}{8}$			
RI-D6					$\frac{45}{64}$	$\frac{39}{256}$	$-\frac{1}{256}$		
RI-D8					$\frac{175}{256}$	$\frac{505}{3072}$	$-\frac{5}{768}$	$\frac{1}{3072}$	
RI-D10					$\frac{11250}{16384}$	$\frac{22435}{131072}$	$-\frac{1085}{131072}$	$\frac{91}{131072}$	$-\frac{5}{131072}$
RI-N2					1				
RI-N4	$\frac{3}{4}$				$\frac{1}{8}$				
RI-N6	$\frac{1}{46}$				$\frac{15}{23}$	$\frac{9}{46}$			
RI-N8	$\frac{1}{22}$				$\frac{105}{176}$	$\frac{171}{704}$	$\frac{3}{704}$		
RI-N10	$\frac{38}{563}$	$\frac{1}{1126}$			$\frac{315}{563}$	$\frac{625}{2252}$	$\frac{25}{2252}$		

where

$$f_{i+1} = f(u_{i+1}) = cu_{i+1}, \quad f_{i+1/2} = cu^L_{i+1/2}, \tag{47}$$

where $u^L_{i+1/2}$ can be obtained through interpolation schemes, such as Eq.(41) for linear problems. While, in the present paper, $u^L_{i+1/2}$ is computed through RI schemes indicated by Eq.(43). Here the RI-D6 is used as illustration.

$$u^L_{i+1/2} = \frac{45}{64}\tilde{u}^L_{i+1/2} + \frac{39}{256}\left(u_i + u_{i+1}\right) - \frac{1}{256}\left(u_{i-1} + u_{i+2}\right), \tag{48}$$

where $\tilde{u}^L_{i+1/2}$ can be obtained through reconstruction schemes, such as Eq.(39) for linear problems.

If Eq.(48) is substituted into Eq.(47), and the obtained equation is then substituted into Eq.(46), we will obtain

$$\begin{aligned}\frac{\partial f}{\partial \xi} &= \frac{64}{45}\left\{c\left[\frac{45}{64}\tilde{u}^L_{i+1/2} + \frac{39}{256}\left(u_i + u_{i+1}\right) - \frac{1}{256}\left(u_{i-1} + u_{i+2}\right)\right]\right. \\ &\qquad \left. -c\left[\frac{45}{64}\tilde{u}^L_{i-1/2} + \frac{39}{256}\left(u_{i-1} + u_i\right) - \frac{1}{256}\left(u_{i-2} + u_{i+1}\right)\right]\right\} \\ &\quad - \frac{2}{9}\left(cu_{i+1} - cu_{i-1}\right) + \frac{1}{180}\left(cu_{i+2} - cu_{i-2}\right), \\ &= c\left(\tilde{u}^L_{i+1/2} - \tilde{u}^L_{i-1/2}\right),\end{aligned} \tag{49}$$

which means that the FC-to-C-D6 and RI-D6 will cancel out each other, because the $f = cu$ is linear with u. This indicates that the interpolation schemes through RI adapters is meaningless to linear wave problems. In these problems, directly adopting the reconstruction schemes is simple and efficient.

3.6 Application to 1D Inviscid Burgers' Equation

The one-dimensional (1D) inviscid Burgers' equation has the following form

$$\frac{\partial u}{\partial t} + \frac{\partial f(u)}{\partial x} = 0, \tag{50}$$

where $f = u^2/2$, and $\partial f/\partial u = u$. The above equation can be discretized as

$$\frac{\partial u}{\partial t} = -\frac{\partial f}{\partial x} = -\frac{1}{\Delta x}\frac{\partial f}{\partial \xi}, \tag{51}$$

where $\partial f/\partial \xi$ is computed by Eq.(40). Here we use FC-to-C-D6 for example

$$\frac{\partial f}{\partial \xi} = \frac{64}{45}\left(f_{i+1/2} - f_{i-1/2}\right) - \frac{2}{9}\left(f_{i+1} - f_{i-1}\right) + \frac{1}{180}\left(f_{i+2} - f_{i-2}\right), \tag{52}$$

where

$$\begin{aligned} f_{i+1} &= f(u_{i+1}) = \frac{1}{2}u_{i+1}^2, \\ f_{i+1/2} &= f(u_{i+1/2}^L, u_{i+1/2}^R) = \begin{cases} f(u_{i+1/2}^L) = \frac{1}{2}(u_{i+1/2}^L)^2, & \text{if } \frac{u_{i+1/2}^L + u_{i+1/2}^R}{2} \le 0 \\ f(u_{i+1/2}^R) = \frac{1}{2}(u_{i+1/2}^R)^2, & \text{otherwise} \end{cases}, \end{aligned} \tag{53}$$

where $u_{i+1/2}^L$ is computed through RI schemes indicated by Eq.(43). Here the RI-D6 is used as illustration.

$$u_{i+1/2}^L = \frac{45}{64}\tilde{u}_{i+1/2}^L + \frac{39}{256}\left(u_i + u_{i+1}\right) - \frac{1}{256}\left(u_{i-1} + u_{i+2}\right), \tag{54}$$

where $\tilde{u}_{i+1/2}^L$ can be obtained through reconstruction schemes, such as Eq.(39) for linear problems. The other terms in Eq.(52) and Eq.(53), which are f_{i-1}, $f_{i-1/2}$, f_{i+2}, f_{i-2}, and $u_{i+1/2}^R$, can be computed in similar ways.

It can be seen that the FC-to-C and RI schemes will not cancel out each other anymore, because of the nonlinear flux $f = u^2/2$. The above procedures can be directly extended to three-dimensional problems in high order, which is to be discussed in the next section for CCFDM.

3.7 Application to 3D Euler/Navier-Stokes Equations

To begin with, the convective term $\partial \hat{E}/\partial \xi$ in Eq.(15) is focused in this section. The discretization has been shown in Eq.(17), Eq.(18) and Eq.(19). Here, the FC-to-C-D6 is chosen as illustration, which has the following form.

$$\left.\frac{\partial \hat{E}}{\partial \xi}\right|_i = \frac{64}{45}(\hat{E}_{i+1/2} - \hat{E}_{i-1/2}) - \frac{2}{9}(\hat{E}_{i+1} - \hat{E}_{i-1}) + \frac{1}{180}(\hat{E}_{i+2} - \hat{E}_{i-2}). \tag{55}$$

As shown in Eq.(20) and Eq.(21), the flux at face centers can be calculated by arbitrary approximate Riemann solver, and the flux at cell centers can be directly calculated. To be specific, they are

$$\begin{aligned} \text{face: } \hat{E}_{i+1/2} &= Roe(Q_{i+1/2}^L, Q_{i+1/2}^R, J\xi_x, J\xi_y, J\xi_z), \\ \text{cell: } \hat{E}_{i+1} &= \begin{pmatrix} \rho U \\ \rho u U + pJ\xi_x \\ \rho v U + pJ\xi_y \\ \rho w U + pJ\xi_z \\ (\rho e + p)U \end{pmatrix}_{i+1}, \end{aligned} \tag{56}$$

where $U = uJ\xi_x + vJ\xi_y + wJ\xi_z$, and $Q_{i+1/2}^L$ is obtained from the RI schemes indicated by Eq.(43). We still choose the RI-D6 for illustration

$$Q_{i+1/2}^L = \frac{45}{64}\tilde{Q}_{i+1/2}^L + \frac{39}{256}\left(Q_i + Q_{i+1}\right) - \frac{1}{256}\left(Q_{i-1} + Q_{i+2}\right), \tag{57}$$

where $\tilde{Q}_{i+1/2}^L$ can be obtained through reconstruction schemes, such as Eq.(39) for linear problems.

Note that not only the conservative variables Q can be used above, but also the primitive variables and the characteristic variables can be adopted.

In the following subsections, three well-optimized high-order high-resolution nonlinear reconstruction schemes are introduced in the present paper for this $\tilde{Q}_{i+1/2}^L$.

3.7.1 WENO-CU6 from Hu et al.

The WENO-CU6 reconstruction scheme from Hu et al. [8] is used in the present research with the following form

$$\tilde{Q}^L_{i+1/2} = \sum_{k=0}^{3} \omega_k \tilde{Q}^L_{i+1/2,k} \tag{58}$$

where the schemes on the sub-stencils are

$$\begin{aligned}
\tilde{Q}^L_{i+1/2,0} &= \frac{1}{3}Q_{i-2} - \frac{7}{6}Q_{i-1} + \frac{11}{6}Q_i, \\
\tilde{Q}^L_{i+1/2,1} &= -\frac{1}{6}Q_{i-1} + \frac{5}{6}Q_i + \frac{1}{3}Q_{i+1}, \\
\tilde{Q}^L_{i+1/2,2} &= \frac{1}{3}Q_i + \frac{5}{6}Q_{i+1} - \frac{1}{6}Q_{i+2}, \\
\tilde{Q}^L_{i+1/2,3} &= \frac{11}{6}Q_{i+1} - \frac{7}{6}Q_{i+2} + \frac{1}{3}Q_{i+3}.
\end{aligned} \tag{59}$$

The nonlinear weights are calculated by

$$\omega_k = \frac{\alpha_k}{\sum_{k=0}^{3}\alpha_k}, \quad \alpha_k = d_k\left(C + \frac{\tau_6}{\beta_k + \epsilon}\right), \tag{60}$$

where $\epsilon = 10^{-40}$, $C = 20$ and

$$\begin{aligned}
\beta_0 &= \frac{1}{4}(Q_{i-2} - 4Q_{i-1} + 3Q_i)^2 &&+\frac{13}{12}(Q_{i-2} - 2Q_{i-1} + Q_i)^2, \\
\beta_1 &= \frac{1}{4}(Q_{i-1} - Q_{i+1})^2 &&+\frac{13}{12}(Q_{i-1} - 2Q_i + Q_{i+1})^2, \\
\beta_2 &= \frac{1}{4}(3Q_i - 4Q_{i+1} + Q_{i+2})^2 &&+\frac{13}{12}(Q_i - 2Q_{i+1} + Q_{i+2})^2.
\end{aligned} \tag{61}$$

The additional β_3 for the downwind stencil is calculated by

$$\begin{aligned}
\beta_3 = \beta_6 = \frac{1}{10080} \\
&[Q_{i-2}(271779Q_{i-2} + 2380800Q_{i-1} + 4086352Q_i - 3462252Q_{i+1} + 1458762Q_{i+2} - 245620Q_{i+3}) \\
&+ Q_{i-1}(5653317Q_{i-1} - 20427884Q_i + 17905032Q_{i+1} - 7727988Q_{i+2} + 1325006Q_{i+3}) \\
&+ Q_i(19510972Q_i - 35817664Q_{i+1} + 15929912Q_{i+2} - 2792660Q_{i+3}) \\
&+ Q_{i+1}(17195652Q_{i+1} - 15880404Q_{i+2} + 2863984Q_{i+3}) \\
&+ Q_{i+2}(3824847Q_{i+2} - 1429976Q_{i+3}) \\
&+ 139633Q^2_{i+3}].
\end{aligned} \tag{62}$$

The global τ_6 has the following form

$$\tau_6 = \left|\beta_6 - \frac{1}{6}(\beta_0 + 4\beta_1 + \beta_2)\right|. \tag{63}$$

And the optimal weights depend on

$$d_0 = \frac{1}{20}, \quad d_1 = \frac{9}{20}, \quad d_2 = \frac{9}{20}, \quad d_3 = \frac{1}{20}. \tag{64}$$

All the above equations form the WENO-CU6 scheme. When all the stencils are smooth enough, this scheme will become

$$\tilde{Q}_{i+1/2} = \frac{1}{60}(Q_{i-2} - 8Q_{i-1} + 37Q_i + 37Q_{i+1} - 8Q_{i+2} + Q_{i+3}). \tag{65}$$

In the following section, the reconstruction scheme WENO-CU6 is transformed into interpolation scheme through RI-D6. The resulting interpolation scheme with CCFDM is then compared with the original reconstruction scheme with cell-centered finite volume method.

Note that the interpolation version of WENO-CU6, which is the WCNS-CU6, has been proposed in [23][24][25]. However, the RI schemes are still useful for those solvers with WENO-CU6 available.

3.7.2 WGVC-WENO7 from He et al.

The WGVC-WENO7 scheme proposed by He et al. [26] is a hybrid scheme of weighted group velocity control (WGVC) scheme and WENO scheme. The WGVC-WENO7 scheme is formed by weighting four sub-schemes. To begin with, we have the following equation

$$\tilde{Q}^L_{i+1/2} = \sum_{k=0}^{3} \omega_k \tilde{Q}^L_{i+1/2,k} \tag{66}$$

where the schemes on the sub-stencils are

$$\begin{aligned}
\tilde{Q}^L_{i+1/2,0} &= \frac{1}{12}(-3Q_{i-3} + 13Q_{i-2} - 23Q_{i-1} + 25Q_i),\\
\tilde{Q}^L_{i+1/2,1} &= \frac{1}{12}(Q_{i-2} - 5Q_{i-1} + 13Q_i + 3Q_{i+1}),\\
\tilde{Q}^L_{i+1/2,2} &= \frac{1}{12}(-Q_{i-1} + 7Q_i + 7Q_{i+1} - Q_{i+2}),\\
\tilde{Q}^L_{i+1/2,3} &= \frac{1}{12}(3Q_i + 13Q_{i+1} - 5Q_{i+2} + Q_{i+3}).
\end{aligned} \tag{67}$$

The nonlinear weights are defined by

$$\begin{aligned}
\omega_0 &= (1-\theta)\cdot(0.0882\varpi_m) &&+\theta\cdot\omega_0^{WENO},\\
\omega_1 &= (1-\theta)\cdot(0.2 + 0.441\varpi_m) &&+\theta\cdot\omega_1^{WENO},\\
\omega_2 &= (1-\theta)\cdot(0.6 - 0.2646\varpi_m) &&+\theta\cdot\omega_2^{WENO},\\
\omega_3 &= (1-\theta)\cdot(0.2 - 0.2646\varpi_m) &&+\theta\cdot\omega_3^{WENO}.
\end{aligned} \tag{68}$$

where

$$\theta(s) = s^q\cdot(q+1-q\cdot s),\quad s = 1 - \frac{\varpi_m\varpi_s}{D_m D_s}. \tag{69}$$

In the above equations,

$$q = 100,\quad D_m = \frac{1000}{3087},\quad D_s = \frac{2087}{3087}, \tag{70}$$

$$\varpi_m = \frac{\gamma_m}{\gamma_m+\gamma_s},\quad \varpi_s = \frac{\gamma_s}{\gamma_m+\gamma_s}, \tag{71}$$

$$\gamma_m = D_m(1 + (\frac{\tau}{\beta_0} + \epsilon)^p),\quad \gamma_s = D_s(1 + (\frac{\tau}{\beta_3} + \epsilon)^p), \tag{72}$$

$$\tau = |\beta_0 - \beta_3|. \tag{73}$$

The WENO7 related weights in Eqs.(68) is defined by

$$\omega_k^{WENO} = \frac{\alpha_k}{\sum_{k=0}^{3}\alpha_k},\quad \alpha_k = \frac{c_k}{(\beta_k+\epsilon)^p}, \tag{74}$$

$$\epsilon = 10^{-6},\quad p = 2, \tag{75}$$

The smoothness indicator for the original WENO7 is defined by

$$\begin{aligned}
\beta_0 &= Q_{i-3}(547Q_{i-3} - 3882Q_{i-2} + 4642Q_{i-1} - 1854Q_i)\\
&\quad + Q_{i-2}(7043Q_{i-2} - 17246Q_{i-1} + 7042Q_i) + Q_{i-1}(11003Q_{i-1} - 9402Q_i) + 2107Q_i^2,\\
\beta_1 &= Q_{i-2}(267Q_{i-2} - 1642Q_{i-1} + 1602Q_i - 494Q_{i+1})\\
&\quad + Q_{i-1}(2843Q_{i-1} - 5966Q_i + 1922Q_{i+1}) + Q_i(3443Q_i - 2522Q_{i+1}) + 547Q_{i+1}^2,\\
\beta_2 &= Q_{i-1}(547Q_{i-1} - 2522Q_i + 1922Q_{i+1} - 494Q_{i+2})\\
&\quad + Q_i(3443Q_i - 5966Q_{i+1} + 1602Q_{i+2}) + Q_{i+1}(2843Q_{i+1} - 1642Q_{i+2}) + 267Q_{i+2}^2,\\
\beta_3 &= Q_i(2107Q_i - 9402Q_{i+1} + 7042Q_{i+2} - 1854Q_{i+3})\\
&\quad + Q_{i+1}(11003Q_{i+1} - 17246Q_{i+2} + 4642Q_{i+3}) + Q_{i+2}(7043Q_{i+2} - 3882Q_{i+3}) + 547Q_{i+3}^2.
\end{aligned} \tag{76}$$

And the optimal weights for WENO depend on

$$c_0 = \frac{1}{35},\ \ c_1 = \frac{12}{35},\ \ c_2 = \frac{18}{35},\ \ c_3 = \frac{4}{35}. \tag{77}$$

In this paper, the WGVC-WENO7 scheme is used in combination with RI-D8 scheme for CCFDM.

3.7.3 OMP6 from Li et al.

The sixth-order monotonicity-preserving optimized scheme (OMP6) proposed by Li et al. [27] is adopted in this paper. Detailed equations are as follows.

$$\tilde{Q}^{L}_{i+1/2} = \begin{cases} \tilde{Q}^{Linear}_{i+1/2} & \text{if } \left(\tilde{Q}^{Linear}_{i+1/2} - Q_i\right)\left(\tilde{Q}^{Linear}_{i+1/2} - \tilde{Q}^{MP}_{i+1/2}\right) \le 10^{-10} \\ \tilde{Q}^{Nonlinear}_{i+1/2} & \text{otherwise} \end{cases} \tag{78}$$

where

$$\begin{aligned}
\tilde{Q}^{Linear}_{i+1/2} &= \frac{3}{6000}Q_{i+4} + \frac{79}{6000}Q_{i+3} - \frac{737}{6000}Q_{i+2} + \frac{3595}{6000}Q_{i+1} + \frac{3805}{6000}Q_i - \frac{863}{6000}Q_{i-1} \\
&\quad + \frac{121}{6000}Q_{i-2} - \frac{3}{6000}Q_{i-3}, \\
\tilde{Q}^{Nonlinear}_{i+1/2} &= \tilde{Q}^{Linear}_{i+1/2} + minmod\left(\tilde{Q}^{min}_{i+1/2} - \tilde{Q}^{Linear}_{i+1/2}, \tilde{Q}^{max}_{i+1/2} - \tilde{Q}^{Linear}_{i+1/2}\right), \\
\tilde{Q}^{MP}_{i+1/2} &= \tilde{Q}^{Linear}_{i+1/2} + minmod\left[Q_{i+1} - Q_i, 4(Q_i - Q_{i-1})\right], \\
\tilde{Q}^{min}_{i+1/2} &= max\left[min\left(Q_i, Q_{i+1}, \tilde{Q}^{MD}_{i+1/2}\right), min\left(Q_i, \tilde{Q}^{UL}_{i+1/2}, \tilde{Q}^{LC}_{i+1/2}\right)\right], \\
\tilde{Q}^{max}_{i+1/2} &= min\left[max\left(Q_i, Q_{i+1}, \tilde{Q}^{MD}_{i+1/2}\right), max\left(Q_i, \tilde{Q}^{UL}_{i+1/2}, \tilde{Q}^{LC}_{i+1/2}\right)\right], \\
\tilde{Q}^{MD}_{i+1/2} &= \frac{1}{2}\left(Q_i + Q_{i+1}\right) - \frac{1}{2}d^{M}_{i+1/2}, \\
\tilde{Q}^{UL}_{i+1/2} &= Q_i + 4\left(Q_i - Q_{i-1}\right), \\
\tilde{Q}^{LC}_{i+1/2} &= \frac{1}{2}\left(3Q_i - Q_{i-1}\right) + \frac{4}{3}d^{M}_{i-1/2}, \\
d^{M}_{i+1/2} &= minmod\left(4Q_i - Q_{i+1}, 4Q_{i+1} - Q_i, Q_i, Q_{i+1}\right), \\
d_i &= Q_{i-1} - 2Q_i + Q_{i+1}.
\end{aligned} \tag{79}$$

In the following sections, the RI-D10 adapter scheme is utilized to convert OMP6 to its interpolation version.

3.7.4 Approximate Dispersion Relation of the Nonlinear Schemes

In this section, the dispersion and dissipation of the implemented nonlinear schemes are analyzed by the approximate dispersion relation (ADR) [28], which is shown in Fig.2. In Fig.2, the interpolation forms of the WENO-CU6, WGVC-WENO7 and OMP6 are compared with their original reconstruction forms. It has to be point out that the ADR technique depends on the 1D linear wave equation, which will make the derived interpolation schemes the very same with the original reconstruction ones. However, when the derived interpolation schemes are applied to nonlinear Euler or Navier-Stokes equations. The numerical results will be different, which can be found in the next section of this paper.

In the comparison of dispersion, the WGVC-WENO7 on the 7-point stencil and the OMP6 on the 8-point stencil are very close to the theoretical dispersion when $k\Delta x < 1.7$. In the wavenumber range of $k\Delta x < 1.3$, the WENO-CU6 on the 6-point stencil is also close to the theoretical dispersion. In high wavenumber range, the OMP6 has the best dispersion.

In the comparison of dissipation, all the three schemes have similar dissipation with theoretical dissipation when $k\Delta x < 1.3$. The WENO-CU6 has almost the best dissipation, except that the WGVC-WENO7 is slightly better in the range of $1.5 < k\Delta x < 2.1$. And the OMP6 has the largest dissipation in high wavenumber range.

The explanation to the observations is simple. Both WGVC-WENO7 and OMP6 are dispersion optimized at the cost of the schemes' orders lower than the highest achievable orders. And the WENO-CU6 is optimized through adding a downwind global stencil to make the upwind stencil central. Thus, the dispersion optimized WGVC-WENO7 and OMP6 have very good dispersion, and the dissipation optimized WENO-CU6 has attractive dissipation.

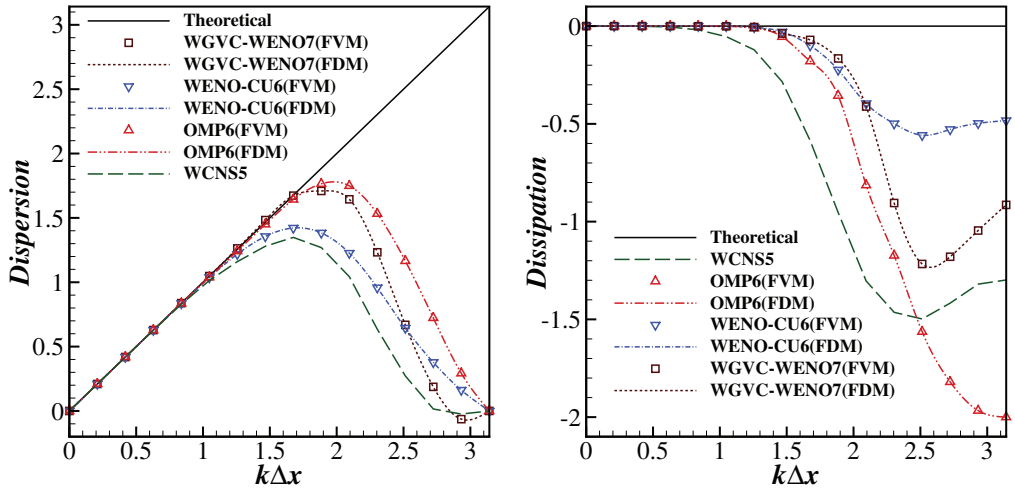

(a) Dispersion (b) Dissipation

Figure 2: ADR of the WENO-CU6, WGVC-WENO7 and OMP6

3.8 Further Discussion on CCFDM and CCSCMM

In this section, the relation between CCFDM and finite volume method (FVM) is briefly discussed by focusing on the geometric metrics and Jacobian. In the following discussion, 2nd-order linear central schemes are utilized for the geometric discretization, which include

$$
\begin{aligned}
(\cdot)'_i &= (\cdot)_{i+1/2} - (\cdot)_{i-1/2}, \\
(\cdot)_i &= \frac{1}{2}\big[(\cdot)_{i+1/2} + (\cdot)_{i-1/2}\big].
\end{aligned}
\tag{80}
$$

First, the metrics on the red surface in Fig. 3 calculated by Eq. (23) can be discretized in the following

form

$$
\begin{aligned}
(J\xi_x)^{S1} &= \underbrace{\delta_2^{\zeta}(\underset{edge-\eta}{z}\underbrace{\delta_3^{\eta}\underset{node}{y}}_{edge-\eta})}_{face-\eta\zeta} - \underbrace{\delta_2^{\eta}(\underset{edge-\zeta}{z}\underbrace{\delta_3^{\zeta}\underset{node}{y}}_{edge-\zeta})}_{face-\eta\zeta} \\
&= \underbrace{\Big[(\underset{edge-\eta}{z}\underbrace{\delta_3^{\eta}\underset{node}{y}}_{edge-\eta})\Big|_F - (\underset{edge-\eta}{z}\underbrace{\delta_3^{\eta}\underset{node}{y}}_{edge-\eta})\Big|_H\Big]}_{face-\eta\zeta} - \underbrace{\Big[(\underset{edge-\zeta}{z}\underbrace{\delta_3^{\zeta}\underset{node}{y}}_{edge-\zeta})\Big|_E - (\underset{edge-\zeta}{z}\underbrace{\delta_3^{\zeta}\underset{node}{y}}_{edge-\zeta})\Big|_G\Big]}_{face-\eta\zeta} \\
&= \underbrace{\big[z_F(y_B - y_C) - z_H(y_A - y_D)\big]}_{face-\eta\zeta} - \underbrace{\big[z_E(y_B - y_A) - z_G(y_C - y_D)\big]}_{face-\eta\zeta} \\
&= \frac{z_B + z_C}{2}(y_B - y_C) - \frac{z_A + z_D}{2}(y_A - y_D) - \frac{z_A + z_B}{2}(y_B - y_A) + \frac{z_C + z_D}{2}(y_C - y_D) \\
&= \frac{1}{2}\big[(y_A - y_C)(z_B - z_D) - (y_B - y_D)(z_A - z_C)\big].
\end{aligned}
\tag{81}
$$

Similarly, the following equations can be obtained

$$
\begin{aligned}
(J\xi_y)^{S1} &= \frac{1}{2}\big[(x_B - x_D)(z_A - z_C) - (x_A - x_C)(z_B - z_D)\big], \\
(J\xi_z)^{S1} &= \frac{1}{2}\big[(x_A - x_C)(y_B - y_D) - (x_B - x_D)(y_A - y_C)\big],
\end{aligned}
\tag{82}
$$

which indicate

$$
\big(J\xi_x, J\xi_y, J\xi_z\big)^{S1} = \frac{1}{2}\overrightarrow{CA} \times \overrightarrow{DB} = \big(S_x, S_y, S_z\big)^{\mathrm{FVM}},
\tag{83}
$$

which means that 2nd-order surface metrics are exactly the same with the surface vector of FVM in numeric.

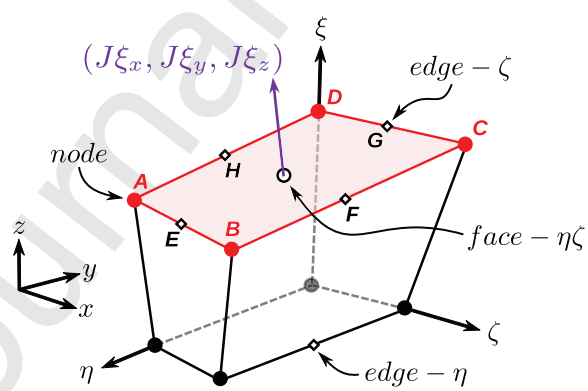

Figure 3: Metrics on $face-\eta\zeta$. Note that the cell center is not illustrated.

Second, consider the following equation which adopts the Green-Gauss equation

$$
\oiint_{\partial\Omega}(x, y, z)d\overrightarrow{S} = \iiint_{\Omega}\nabla\cdot(x, y, z)dV = \iiint_{\Omega}\Big(\frac{\partial x}{\partial x} + \frac{\partial y}{\partial y} + \frac{\partial z}{\partial z}\Big)dV = 3V,
\tag{84}
$$

where V is the cell volume. When the 2nd-order central difference scheme and the above Eq.(83) are applied to Eq.(26), the following relation can be obtained

$$
J = V = \sum_{f\in\partial\Omega}(x_f, y_f, z_f)\overrightarrow{S}_f,
\tag{85}
$$

where $\overrightarrow{S}_f$ is in the outward normal direction. Note that, the sum of surface integration in outward normal direction in FVM can be regard as the difference of surface variables in uniform normal direction in CCFDM. This further indicates that the 2nd-order Jacobian is exactly identical to the volume of FVM in numeric.

The above discussion with Eq.(83) and Eq.(85) lays the foundation that cell-centered FVM can be realized through CCFDM with 2nd-order geometric discretization. Because both FVM and CCFDM can be concluded into three main steps in spatial-discretization:

- step 1: cell-to-face reconstruction/interpolation of primitive/conservative/characteristic variables;
- step 2: approximate Riemann solver for flux variables on the faces;
- step 3: face-to-cell difference for the derivatives of flux variables.

This further indicates that those finite volume solvers on structured grids can be "UPGRADED" to high-order CCFDM with the most of the algorithms and codes reused without further modification, such as boundary condition, time-advancing, pre/post-treat methods, etc. To be specific, three main steps have to be taken:

- step 1: replace reconstruction scheme with interpolation scheme, or use RI scheme to make one;
- step 2: replace difference scheme of FVM with those F-to-C/FC-to-C difference schemes of CCFDM;
- step 3: replace surface vectors and volumes of cells with surface metrics and Jacobians of cells.

Note that as is pointed out by Titarev and Toro [29], the FVM without Gaussian integration of flux on the surface is 2nd-order only. However, in the simulation with relative good quality of grids, the high-resolution property of the reconstruction scheme could still be remained in this FVM, which will be shown in the following section.

Finally, two working modes are developed: the 2nd-order FVM mode and the high-order FDM mode. Both modes are realized through CCFDM and CCSCMM, the details of which are listed in Table 4.

Table 4: The 2nd-order FVM and the high-order FDM realized through CCFDM

Working Mode	2nd-order FVM	high-order FDM
Geometric Schemes	$(\cdot)'_i = (\cdot)_{i+1/2} - (\cdot)_{i-1/2}$ $(\cdot)_i = \frac{1}{2}\left[(\cdot)_{i+1/2} + (\cdot)_{i-1/2}\right]$	high-order F-to-C/FC-to-C difference high-order central interpolation
Geometric Variables	Surface Vector: (S_x, S_y, S_z) Volume of Cell: V	Surface Metrics: $(J\xi_x, J\xi_y, J\xi_z)$ etc. Jacobian of Cell: J
Cell-to-Face Scheme (Pimitive/Characteristic)	Reconstruction	Interpolation
Flux at Face	Roe, AUSM, SLAU, HLLC, etc.	
Face-to-Cell Difference (Flux)	$(\cdot)'i = (\cdot)_{i+1/2} - (\cdot)_{i-1/2}$	high-order F-to-C/FC-to-C difference

The present paper is a step forward that the interpolation schemes do not have to be totally re-derived, whereas they can be obtained from the available reconstruction schemes through RI adapter schemes, which further makes the reconstruction schemes reusable in the FDM mode. In the following section, the derived CCFDM with reconstruction schemes and RI adapters are in "high-order" mode of CCFDM, while the original reconstruction schemes are adopted through the "2nd-order FVM" mode of CCFDM. Detailed schemes used are listed in Table5.

4 Verification

In this section, the derived high-order schemes with corresponding adapters are verified through a series of benchmark cases in comparison with their 2nd-order FVM forms. The verification includes both linear and nonlinear problems, both accuracy test and resolution test.

Table 5: Schemes and methods implemented in the following Verification section

Working Mode	Reconstruction Scheme	RI Scheme	Difference of Flux
FVM	WENO-CU6	N/A	F-to-C-2
	WGVC-WENO7	N/A	F-to-C-2
	OMP6	N/A	F-to-C-2
FDM	WENO-CU6	RI-D6	FC-to-C-D6
	WGVC-WENO7	RI-D8	FC-to-C-D8
	OMP6	RI-D10	FC-to-C-D10

In this section, the 3-step 3rd-order TVD Runge-Kutta scheme [5] is used for time advancement.

4.1 Freestream Preservation

Freestream preservation refers to the property that in the simulation without disturbance the flow variables at solution points should remain constants under the condition that these flow variables are constants everywhere initially.

To be specific, in the problem with farfield boundary conditions only, initialize the simulation domain with uniform freestream parameters. If the flow variables could remain freestream parameters after long time simulation, then freestream is considered to be preserved.

Freestream preservation is the basic requirement to CFD discretization methods. The non-preserved freestream from discretization error may result in nonphysical fluctuation or even divergence of the simulation. The freestream preservation is usually not satisfied in finite difference method due to the violation of GCL. Thus this benchmark case is chosen to verify method in this paper.

Firstly, a two-dimensional highly wavy grid with 60×60 cells is used. Periodic boundary condition is specified in both directions. The error of pressure at $t = 1$, which is shown in Fig.4 and Table6, is defined by

$$P_{error} = \frac{P - P_0}{P_0}, \tag{86}$$

where $P_0 = 1/1.4$ is the pressure at $t = 0$.

It is quite obvious that without GCL satisfied the error introduced on highly wavy grid is tremendous. And CCSCMM is able to satisfy GCL to obtain physical result.

Table 6: Error of pressure on 2D wavy grid.

Method	$\lvert P_{error}\rvert^{L^1-norm}$	$\lvert P_{error}\rvert^{L^2-norm}$	$\lvert P_{error}\rvert^{L^\infty-norm}$
Non-GCL	$2.894115248602842\times10^{-2}$	$5.367442346553225\times10^{-2}$	$2.969166883808172\times10^{-1}$
GCL(CCSCMM)	$3.790178047956437\times10^{-17}$	$2.414079206411703\times10^{-16}$	$4.440892098500626\times10^{-15}$

Secondly, a three-dimensional grid from the 1st High Lift Prediction Workshop is adopted for the verification of the freestream preservation property in practical 3D configuration. By re-specifying all the "wall" boundary as the "farfield" boundary, freestream should be preserved. The grid topology, iteration residual and contours of pressure errors are displayed in Fig.5. In addition, the pressure errors are also listed in Table 7.

It can be seen that due to the satisfied GCL, the geometry induced error is totally eliminated by CCSCMM, leading to much more physical result in practical simulations.

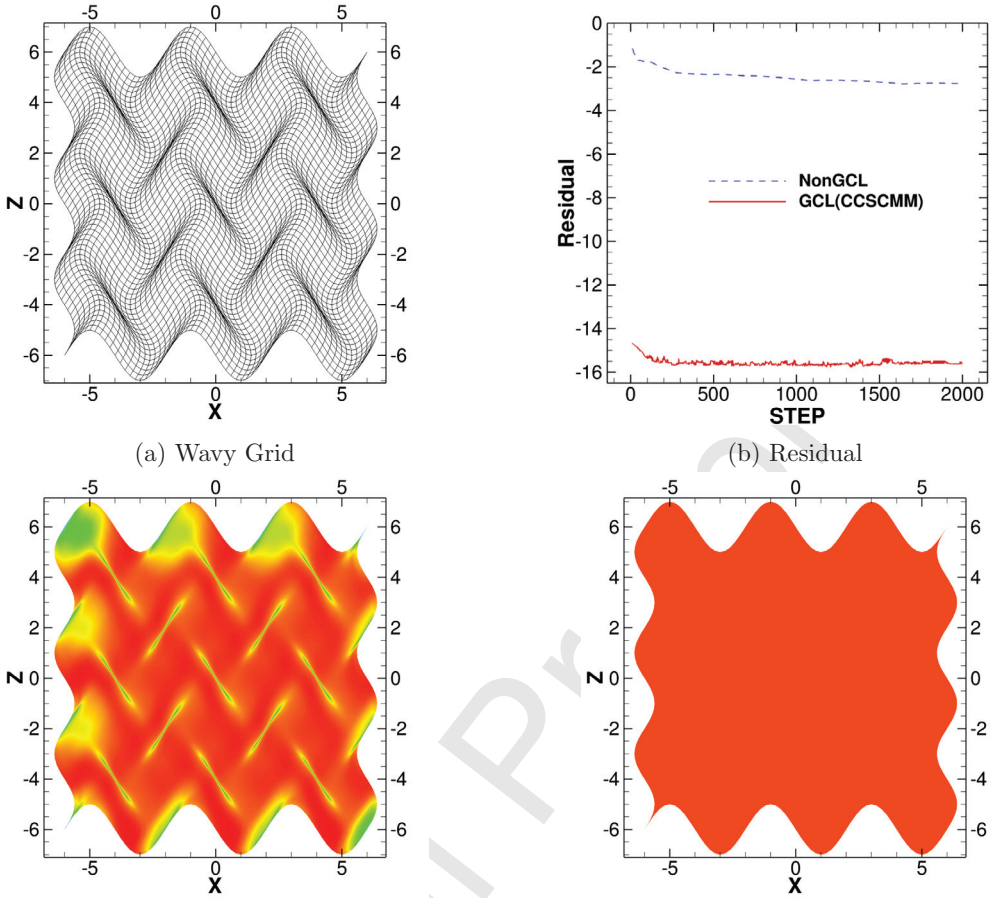

(a) Wavy Grid

(b) Residual

(c) Pressure Error without GCL

(d) Pressure Error with GCL(CCSCMM)

Figure 4: Freestream preservation benchmark on 2D wavy grid. In (c), GCL is violated because metrics are calculated by inversion of coordinate transformation matrix. In (d), GCL is satisfied through CCSCMM.

Table 7: Error of pressure with different geometric method using the High Lift configuration.

Method	$\lvert P_{error}\rvert^{L^1-norm}$	$\lvert P_{error}\rvert^{L^2-norm}$	$\lvert P_{error}\rvert^{L^\infty-norm}$
Non-GCL	$1.818023975514759\times10^{-2}$	$2.488010242753828\times10^{-2}$	$7.397856884418441\times10^{-2}$
GCL(CCSCMM)	$3.645818150301382\times10^{-13}$	$4.913787857526584\times10^{-13}$	$1.942224159279249\times10^{-12}$

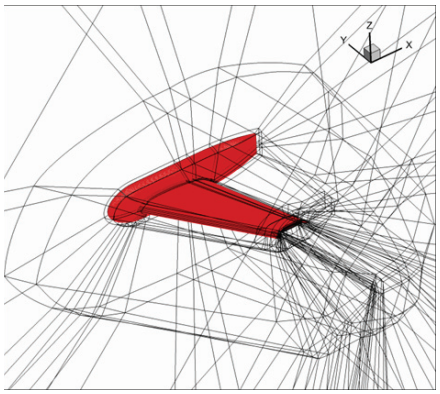

(a) Grid Topology

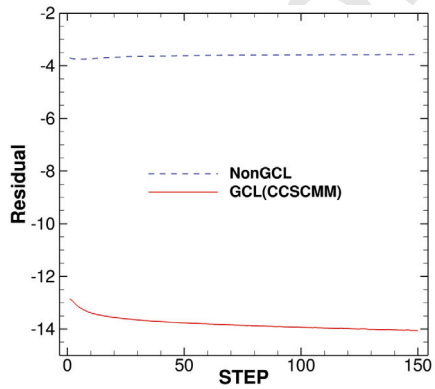

(b) Residual

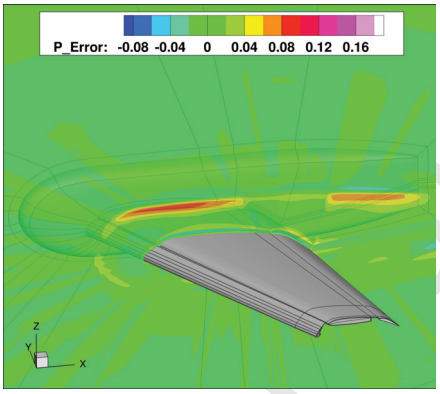

(c) Pressure Error without GCL

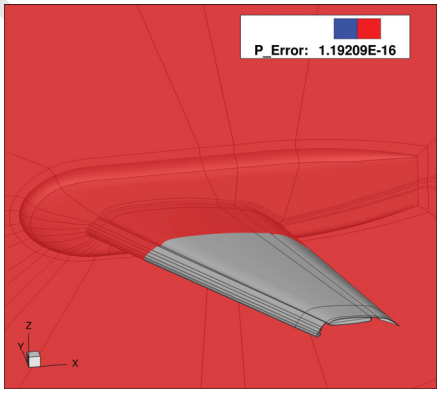

(d) Pressure Error with GCL(CCSCMM)

Figure 5: Freestream preservation benchmark with grid from the 1st High Lift Prediction Workshop. In (a), the "wall" boundary (in red) is re-specified as "farfield" boundary. In (c), GCL is violated because metrics are calculated by inversion of coordinate transformation matrix. In (d), GCL is satisfied through CCSCMM.

4.2 Stationary Isentropic Vortex

This case is utilized to evaluate the order of accuracy of the proposed method on two-dimensional grids. The stationary isentropic vortex is initially located at $(x_c, z_c) = (0, 0)$ with the following conditions

$$\begin{aligned}(u, w) &= \frac{\beta}{2\pi} e^{\left(\frac{1-r^2}{2}\right)} \left[-(z - z_c), (x - x_c)\right], \quad T = 1 - \frac{(\gamma - 1)\beta^2}{8\gamma\pi^2} e^{(1-r^2)}, \\ \rho &= T^{\frac{1}{\gamma-1}}, \quad P = \rho T, \quad r = \sqrt{(x - x_c)^2 + (z - z_c)^2},\end{aligned} \tag{87}$$

where $\beta = 5$ is the strength of the vortex.

Two kinds of grids are adopted: uniform grids and wavy grids. For the uniform grids, the computational domain is $(x, z) \in (-8, 8) \times (-8, 8)$. For the wavy grids, the coordinates are generated by the following equations

$$\begin{aligned}x &= x_{\min} + \Delta x \left[i - 1 + A_x \frac{N}{60} \sin(2\pi\omega) \sin(\frac{\pi B(k-1)}{N})\right], \qquad i = 1, 2, \cdots, N + 1, \\ z &= z_{\min} + \Delta z \left[k - 1 + A_z \frac{N}{60} \sin(2\pi\omega) \sin(\frac{\pi B(i-1)}{N})\right], \qquad k = 1, 2, \cdots, N + 1,\end{aligned} \tag{88}$$

where

$$\begin{aligned}&L = x_{\max} - x_{\min} = z_{\max} - z_{\min}, \quad x_{\min} = z_{\min} = -8, \quad x_{\max} = z_{\max} = 8, \\ &\Delta x = \Delta z = L/N, \quad A_x = 2, \quad A_z = 4, \quad B = 6, \quad \omega = 0.25, \\ &N = 60,\ 80,\ 100,\ 120,\ 140,\ 160.\end{aligned} \tag{89}$$

Periodic boundary condition is specified in both directions. The flow should keep its initial condition at $t > 0$. Thus, the solution at $t = 12$ is compared with initial condition to calculate numerical error. The L^2-norm of density error is defined by the following equation

$$\text{Error}(\rho) = \sqrt{\frac{\Sigma_{i=1}^{N} \Sigma_{j=1}^{N} [\rho_{i,j}(t) - \rho_{i,j}(0)]^2}{N^2}}. \tag{90}$$

There is one thing that should be mentioned. Our finite volume method, which adopts dimensional-by-dimensional discretization without Gaussian integration at faces of cells, ignores the differece between the nodal value at cell centers and the cell-averaged value like most finite volume method, and thus is second-order indeed. In this case on curvilinear grids to evaluate numerical accuracy, the initial values at each cell for the finite volume method is chosen to be the cell-averaged conservative variables. 2D Gaussian integration with 20×20 integration points in each cell is used to calculate the initial cell-averaged conservative variables with the following equations

$$\bar{Q}_{ik} = \frac{1}{S_{ik}} \iint_{\Omega_{ik}} Q(x, z) dS = \frac{\int_{-\frac{\Delta\zeta}{2}}^{\frac{\Delta\zeta}{2}} \int_{-\frac{\Delta\xi}{2}}^{\frac{\Delta\xi}{2}} J(\xi_i + \xi, \zeta_k + \zeta) Q(\xi_i + \xi, \zeta_k + \zeta) d\xi d\zeta}{\int_{-\frac{\Delta\zeta}{2}}^{\frac{\Delta\zeta}{2}} \int_{-\frac{\Delta\xi}{2}}^{\frac{\Delta\xi}{2}} J(\xi_i + \xi, \zeta_k + \zeta) d\xi d\zeta}, \tag{91}$$

where

$$Q = (\rho, \rho u, \rho v, \rho w, \rho e)^T, \quad J(\xi, \zeta) = \begin{vmatrix} \frac{\partial x}{\partial \xi} & \frac{\partial x}{\partial \zeta} \\ \frac{\partial z}{\partial \xi} & \frac{\partial z}{\partial \zeta} \end{vmatrix}, \tag{92}$$

which can be obtained analytically through Eq.(87) and Eq.(88).

The errors of density and the calculated orders of accuracy are shown in Table 8, Table 9 and Fig. 6. It can be seen that the orders of accuracy are very well preserved on the uniform grids, indicating that finite volume methods are 2nd-order only and the finite difference methods are high-order. On the highly wavy grids, the accuracy loss of the finite volume method is very obvious, but the finite difference method could still preserve high-order accuracy.

Finally, the time costs of the derived nonlinear schemes are compared with their original reconstruction ones on the 60×60 grid in Table 10. It can be seen that due to the simplicity of the nonlinear limiter of the OMP6 scheme, it has the fastest speed even though it has the largest scheme stencil.

Table 8: L^2-norm of density error of the stationary isentropic vortex problem on uniform grids.

Cells	Error(ρ) of WENO-CU6		Error(ρ) of WGVC-WENO7		Error(ρ) of OMP6	
	FVM	FDM	FVM	FDM	FVM	FDM
60×60	7.49×10^{-5}	3.54×10^{-6}	9.13×10^{-5}	3.55×10^{-6}	1.14×10^{-4}	4.80×10^{-6}
80×80	4.25×10^{-5}	6.60×10^{-7}	4.99×10^{-5}	5.40×10^{-7}	6.44×10^{-5}	9.24×10^{-7}
100×100	2.73×10^{-5}	1.81×10^{-7}	3.19×10^{-5}	1.21×10^{-7}	4.13×10^{-5}	2.53×10^{-7}
120×120	1.90×10^{-5}	6.12×10^{-7}	2.22×10^{-5}	3.48×10^{-8}	2.88×10^{-5}	8.65×10^{-8}
140×140	1.40×10^{-5}	2.57×10^{-8}	1.63×10^{-5}	1.21×10^{-8}	2.12×10^{-5}	3.48×10^{-8}
160×160	1.07×10^{-5}	1.12×10^{-8}	1.25×10^{-5}	4.81×10^{-9}	1.62×10^{-5}	1.57×10^{-8}
Order	1.98	5.87	2.03	6.73	1.99	5.83

Table 9: L^2-norm of density error of the stationary isentropic vortex problem on wavy grids.

Cells	Error(ρ) of WENO-CU6		Error(ρ) of WGVC-WENO7		Error(ρ) of OMP6	
	FVM	FDM	FVM	FDM	FVM	FDM
60×60	1.03×10^{-3}	8.09×10^{-4}	4.83×10^{-4}	3.31×10^{-4}	2.44×10^{-3}	1.25×10^{-3}
80×80	9.42×10^{-4}	1.56×10^{-4}	4.73×10^{-4}	4.90×10^{-5}	1.56×10^{-3}	1.41×10^{-4}
100×100	6.08×10^{-4}	4.38×10^{-5}	4.39×10^{-4}	1.12×10^{-5}	5.94×10^{-4}	4.83×10^{-5}
120×120	4.52×10^{-4}	1.35×10^{-5}	4.13×10^{-4}	3.73×10^{-6}	3.66×10^{-4}	1.75×10^{-5}
140×140	3.41×10^{-4}	4.87×10^{-6}	3.62×10^{-4}	1.46×10^{-6}	3.49×10^{-4}	7.12×10^{-6}
160×160	2.78×10^{-4}	2.18×10^{-6}	3.03×10^{-4}	6.30×10^{-7}	3.87×10^{-4}	3.30×10^{-6}
Order	1.33	6.03	0.47	6.39	1.87	6.06

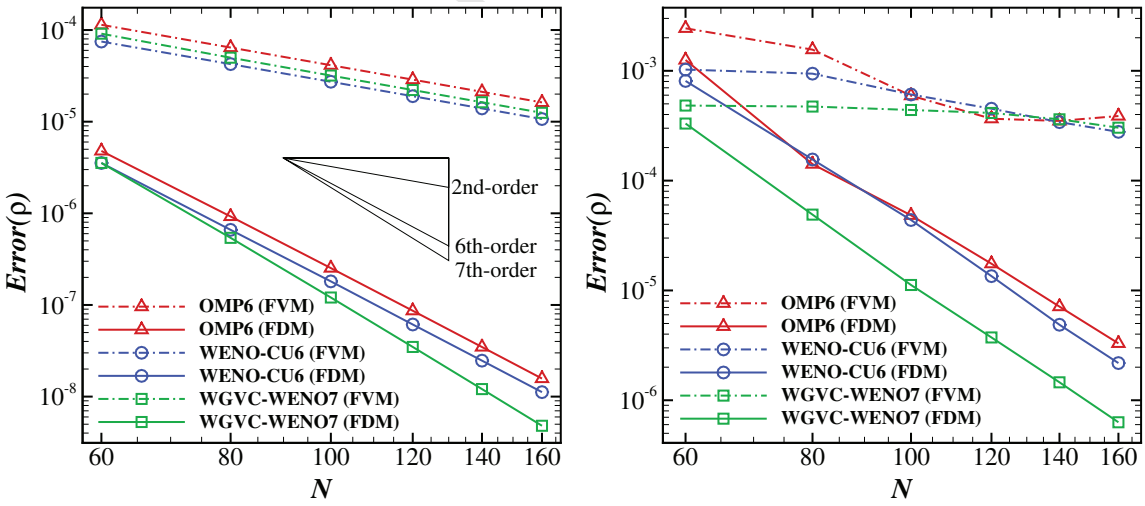

(a) Uniform grids (b) Wavy grids

Figure 6: Order of accuracy of the stationary isentropic vortex problem.

Table 10: Comparison of CPU-time (in seconds) of the isentropic vortex problem on the 60×60 grid.

Methods	CPU-time	Methods	CPU-time	Methods	CPU-time
WENO-CU6(FVM)	103.26	WGVC-WENO7(FVM)	171.38	OMP6(FVM)	65.07
WENO-CU6(FDM)	114.33	WGVC-WENO7(FDM)	182.98	OMP6(FDM)	75.24

4.3 Shu-Osher Problem

The Shu-Osher problem is defined by the following initial condition:

$$(\rho, u, p) = \begin{cases} (3.587143, 2.629369, 10), & \text{if } 0 \le x < 1 \\ (1 + 0.2\sin(5x), 0, 1), & \text{if } 1 \le x \le 10 \end{cases} \tag{93}$$

Firstly, the three nonlinear schemes with their corresponding adapter schemes are simulated for comparison. The density at $t = 1.8$ is obtained in Fig. 7 with 200 cells and in Fig. 8 with 400 cells. It can be seen that the reconstruction schemes are successfully made into the corresponding interpolation ones with very similar performance in resolution.

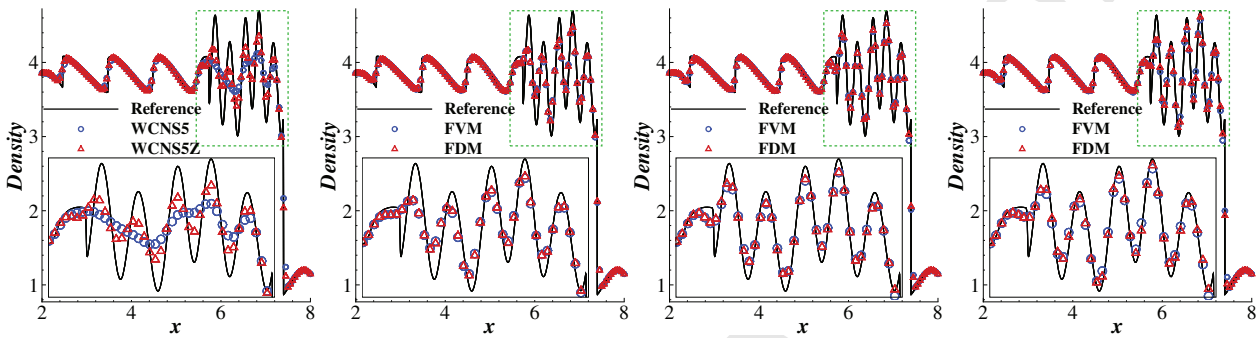

(a) WCNS5(Z) (b) WENO-CU6 (c) WGVC-WENO7 (d) OMP6

Figure 7: Density of Shu-Osher problem at $t = 1.8$ with 200 cells.

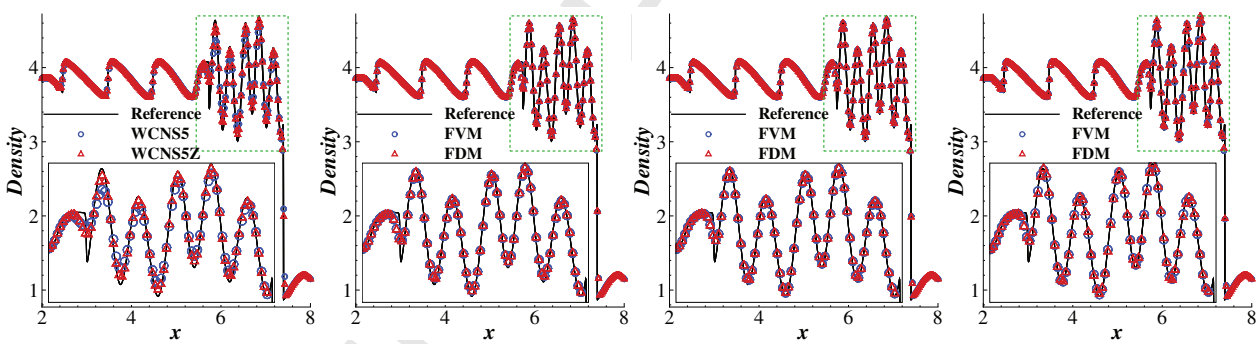

(a) WCNS5(Z) (b) WENO-CU6 (c) WGVC-WENO7 (d) OMP6

Figure 8: Density of Shu-Osher problem at $t = 1.8$ with 400 cells.

Secondly, adapter schemes with different orders are tested for WENO-CU6, WGVC-WENO7 and OMP6 with 200 cells. The results are shown in Fig.9. It can be observed that 2nd-order RI adapter is not able to give acceptable results, while other adapter schemes have similar performance. Another observation is that even if 4th-order RI adapter is used, the 10-point OMP6 is still better than the 6-point WENO-CU6. This indicates that the order and accuracy of adapter scheme will have minor effect on the global performance under the condition that 4th-order or higher-order adapter schemes are adopted.

4.4 Shock tube problem

To demonstrate shock capturing capability, the Sod problem is utilized with the following initial condition

$$(\rho, u, p) = \begin{cases} (1, 0, 1), & \text{if } 0 \le x < 0.5 \\ (0.125, 0, 0.1), & \text{if } 0.5 \le x \le 1 \end{cases} \tag{94}$$

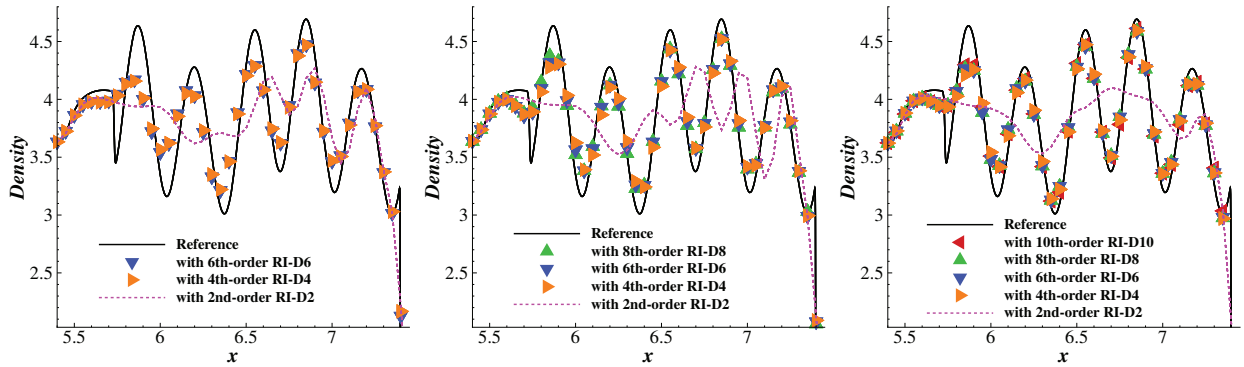

(a) WENO-CU6(200 cells) (b) WGVC-WENO7(200 cells) (c) OMP6(200 cells)

Figure 9: Density of Shu-Osher problem at $t = 1.8$ with different adapter schemes in FDM mode.

The simulation is performed till $t = 0.2$ using 100 cells. Different adapter schemes are chosen for each of these schemes according to the maximum available stencil width.

The calculated density profile is shown in Fig.10. It can be seen that no obvious overshoot or undershoot can be observed, and the adapted interpolation schemes show similar performance in accuracy with the original reconstruction schemes.

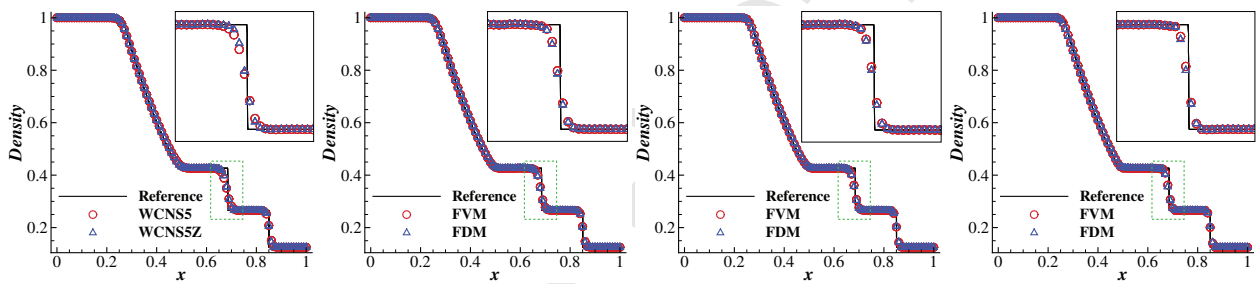

(a) WCNS5(Z) (b) WENO-CU6 (c) WGVC-WENO7 (d) OMP6

Figure 10: Density of Sod problem at $t = 0.2$.

4.5 Shock Wave Impingement on a Spatially Evolving Mixing Layer

This case [30] focuses on the interaction of a reflecting shock wave with shear layer instabilities. The computational domain is $(x, z) \in (0, 200) \times (-20, 20)$. The nonlinear interpolation schemes with adapter schemes are verified in comparison with their reconstruction versions using 500×100 uniformly spaced cells.

The simulated pressure contours at $t = 120$ are demonstrated in Fig.11. It can be found that the adapted interpolated schemes have similar performance in accuracy with the original reconstruction schemes.

4.6 Shock Vortex Interaction

In this case, a moving vortex is passing through a stationary shock located at $x = 0$. The vortex is placed at $(x_v, y_v) = (4, 0)$ at $t = 0$. The initial condition for the flow field is given by the following equations

$$\begin{pmatrix} \rho \\ p \\ \delta u \\ \delta v \end{pmatrix} = \begin{pmatrix} \left(1 - \frac{\gamma-1}{2} M_v^2 e^{1-(r/R)^2}\right)^{\frac{1}{\gamma-1}} \\ \frac{1}{\gamma}\left(1 - \frac{\gamma-1}{2} M_v^2 e^{1-(r/R)^2}\right)^{\frac{\gamma}{\gamma-1}} \\ -M_v e^{\frac{1-(r/R)^2}{2}} (y - y_v) \\ M_v e^{\frac{1-(r/R)^2}{2}} (x - x_v) \end{pmatrix} \tag{95}$$

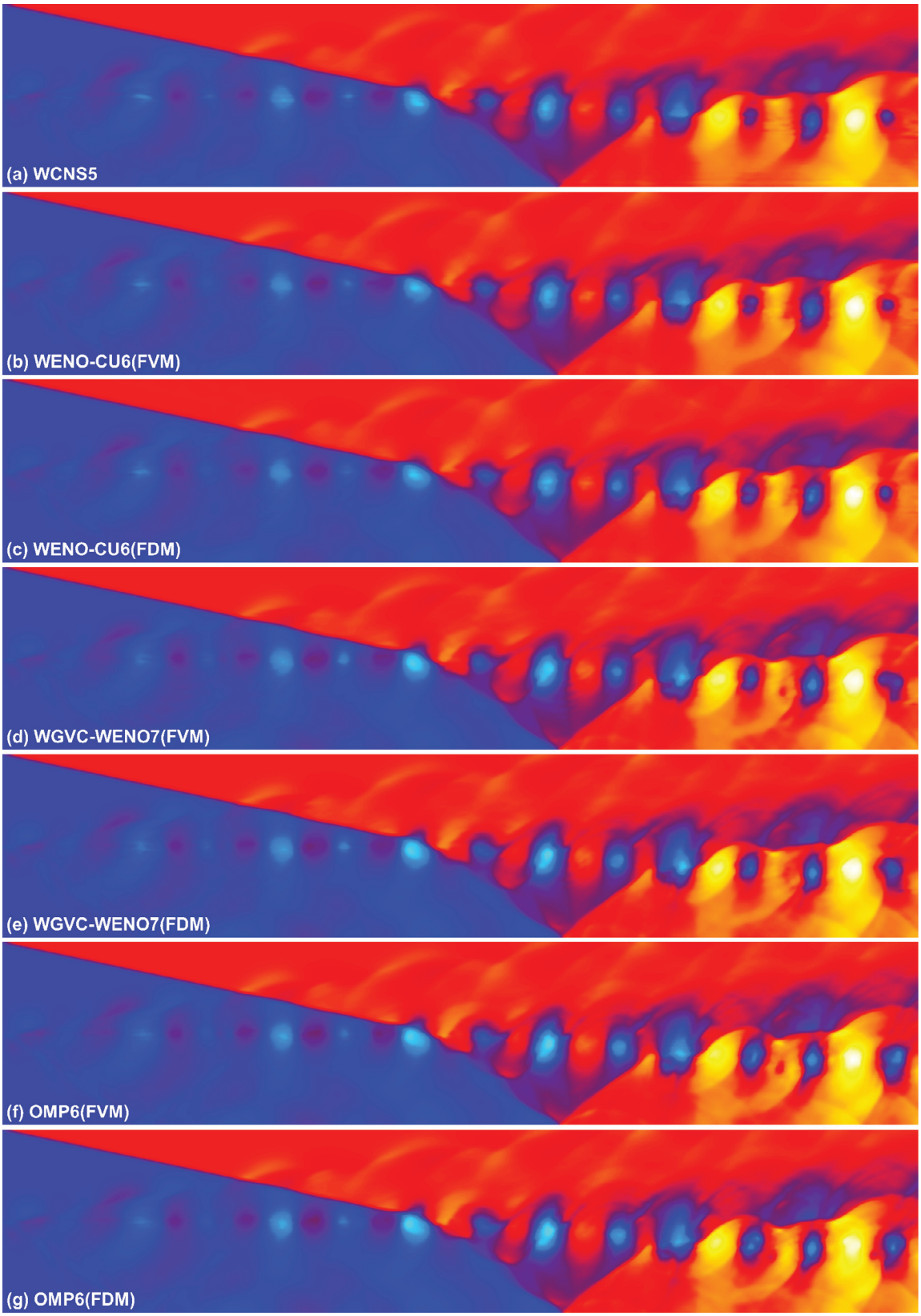

Figure 11: Pressure contours of shock wave impingement on a spatially evolving mixing layer. The contours range from 0.16 to 0.726 with equally spaced 284 levels.

where $\gamma = 1.4$, and $R = 1.0$ is the radius of the vortex. The characteristic Mach number of vortex is $M_v = 1.0$ in this case. The simulation is performed with 600×600 cells in a square domain $[-35, 10] \times [-22.5, 22.5]$ with $\Delta x = \Delta y = \frac{3}{40}$.

The simulated pressure contours of shock vortex interaction problem at $t = 16$ are demonstrated in Fig.12. It can be seen that the results from reconstruction schemes are quite similar to those from interpolation schemes, indicating the effectiveness of adapter schemes.

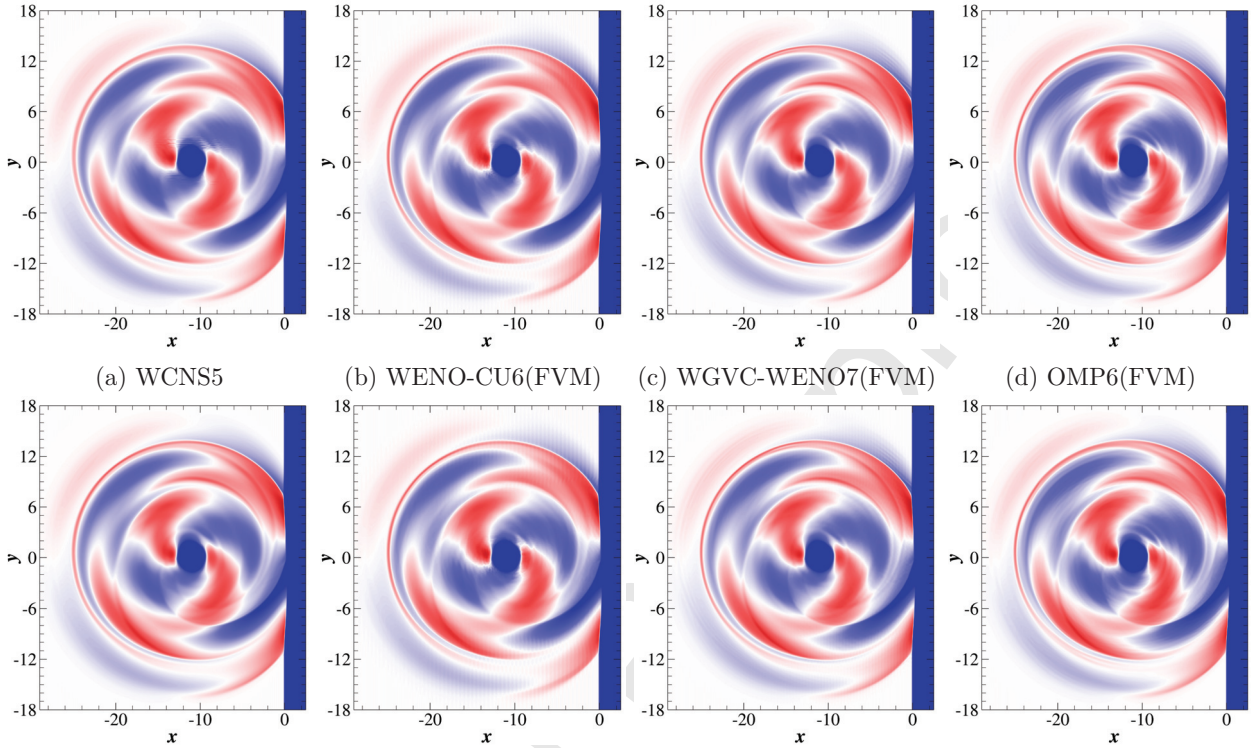

(a) WCNS5 (b) WENO-CU6(FVM) (c) WGVC-WENO7(FVM) (d) OMP6(FVM)

(e) WCNS5Z (f) WENO-CU6(FDM) (g) WGVC-WENO7(FDM) (h) OMP6(FDM)

Figure 12: Pressure contours of shock vortex interaction problem at $t = 16.0$ with 600×600 cells.

5 Conclusion

The present paper develops the high-order high-resolution optimized interpolation schemes for cell-centered finite difference method (CCFDM). This paper proposes that nonlinear reconstruction scheme and nonlinear interpolation scheme can be converted into each other by two series of linear adapter schemes, which include interpolation-to-reconstruction (IR) adapter schemes and reconstruction-to-interpolation (RI) adapter schemes. With the proposed RI adapter schemes, three high-order high-resolution nonlinear reconstruction schemes, which include WENO-CU6, WGVC-WENO7 and OMP6, are transformed into their corresponding interpolation ones. Benchmark cases demonstrate that the RI adapter schemes could mainly preserve the accuracy and robustness of the original well-optimized reconstruction schemes without noticeable increase in computational time cost, indicating the effectiveness and efficiency of the schemes proposed.

Acknowledgment

This work was supported by National Natural Science Foundation of China (Grant No. 91752118, 11672305, 11232011 and 11572331). The authors would like to acknowledge the support from the Strategic Priority Research Program (Grant No. XDB22040104) and the Key Research Program of Frontier Sciences of the Chinese Academy of Sciences (Grant No. QYZDJ-SSW-SYS002).

References

[1] Todd A. Oliver. *A high-order, adaptive, discontinuous Galerkin finite element method for the Reynolds-Averaged Navier-Stokes equations.* Thesis, Massachusetts Institute of Technology, 2008.

[2] H. T. Huynh. A Flux Reconstruction Approach to High-Order Schemes Including Discontinuous Galerkin Methods. American Institute of Aeronautics and Astronautics, June 2007.

[3] Christopher K. W. Tam and Jay C. Webb. Dispersion-Relation-Preserving Finite Difference Schemes for Computational Acoustics. *Journal of Computational Physics*, 107(2):262–281, August 1993.

[4] Guang-Shan Jiang and Chi-Wang Shu. Efficient Implementation of Weighted ENO Schemes. *Journal of Computational Physics*, 126(1):202–228, June 1996.

[5] Xiaogang Deng and Meiliang Mao. Weighted compact high-order nonlinear schemes for the Euler equations. American Institute of Aeronautics and Astronautics, June 1997.

[6] Andrew K. Henrick, Tariq D. Aslam, and Joseph M. Powers. Mapped weighted essentially non-oscillatory schemes: Achieving optimal order near critical points. *Journal of Computational Physics*, 207(2):542–567, August 2005.

[7] Rafael Borges, Monique Carmona, Bruno Costa, and Wai Sun Don. An improved weighted essentially non-oscillatory scheme for hyperbolic conservation laws. *Journal of Computational Physics*, 227(6):3191–3211, March 2008.

[8] X.Y. Hu, Q. Wang, and N.A. Adams. An adaptive central-upwind weighted essentially non-oscillatory scheme. *Journal of Computational Physics*, 229(23):8952–8965, November 2010.

[9] Taku Nonomura, Nobuyuki Iizuka, and Kozo Fujii. Freestream and vortex preservation properties of high-order WENO and WCNS on curvilinear grids. *Computers & Fluids*, 39(2):197–214, February 2010.

[10] Yan Jiang, Chi-Wang Shu, and Mengping Zhang. Free-stream preserving finite difference schemes on curvilinear meshes. *Methods and Applications of Analysis*, 21(1):1–30, 2014.

[11] Taku Nonomura, Daiki Terakado, Yoshiaki Abe, and Kozo Fujii. A new technique for freestream preservation of finite-difference WENO on curvilinear grid. *Computers & Fluids*, 107:242–255, January 2015.

[12] Xiaogang Deng, Yaobing Min, Meiliang Mao, Huayong Liu, Guohua Tu, and Hanxin Zhang. Further studies on geometric conservation law and applications to high-order finite difference schemes with stationary grids. *Journal of Computational Physics*, 239:90–111, 2013.

[13] Taku Nonomura, Seiichiro Morizawa, Hiroshi Terashima, Shigeru Obayashi, and Kozo Fujii. Numerical (error) issues on compressible multicomponent flows using a high-order differencing scheme: Weighted compact nonlinear scheme. *Journal of Computational Physics*, 231(8):3181–3210, April 2012.

[14] Fei Liao, Zhengyin Ye, and Lingxia Zhang. Extending geometric conservation law to cell-centered finite difference methods on stationary grids. *Journal of Computational Physics*, 284:419–433, 2015.

[15] Xiaogang Deng. New High-Order Hybrid Cell-Edge and Cell-Node Weighted Compact Nonlinear Schemes. American Institute of Aeronautics and Astronautics, June 2011.

[16] Taku Nonomura and Kozo Fujii. Robust explicit formulation of weighted compact nonlinear scheme. *Computers & Fluids*, 85:8–18, October 2013.

[17] P.L Roe. Approximate riemann solvers, parameter vectors, and difference schemes. *Journal of Computational Physics*, 43(2):357 – 372, 1981.

[18] Taku Nonomura and Kozo Fujii. Effects of difference scheme type in high-order weighted compact nonlinear schemes. *Journal of Computational Physics*, 228(10):3533–3539, June 2009.

[19] Yoshiaki Abe, Nobuyuki Iizuka, Taku Nonomura, and Kozo Fujii. Conservative metric evaluation for high-order finite difference schemes with the GCL identities on moving and deforming grids. *Journal of Computational Physics*, 232(1):14–21, January 2013.

[20] Yoshiaki Abe, Taku Nonomura, Nobuyuki Iizuka, and Kozo Fujii. Geometric interpretations and spatial symmetry property of metrics in the conservative form for high-order finite-difference schemes on moving and deforming grids. *Journal of Computational Physics*, 260:163–203, 2014.

[21] P. D. Thomas and C. K. Lombard. Geometric Conservation Law and Its Application to Flow Computations on Moving Grids. *AIAA Journal*, 17(10):1030–1037, October 1979.

[22] M. Vinokur and H. C. Yee. Extension of efficient low dissipation high order schemes for 3-D curvilinear moving grids. In *Frontiers of computational fluid dynamics, 2002 (Half Moon Bay, CA, 2000)*, pages 129–164. World Sci. Publ., River Edge, NJ, 2002.

[23] Christoph Brehm, Michael F. Barad, Jeffrey A. Housman, and Cetin C. Kiris. A comparison of higher-order finite-difference shock capturing schemes. *Computers & Fluids*, 122:184–208, November 2015.

[24] Tomohiro Kamiya, Makoto Asahara, and Taku Nonomura. Application of central differencing and low-dissipation weights in a weighted compact nonlinear scheme. *International Journal for Numerical Methods in Fluids*, May 2017.

[25] Man Long Wong and Sanjiva K. Lele. High-order localized dissipation weighted compact nonlinear scheme for shock- and interface-capturing in compressible flows. *Journal of Computational Physics*, 339:179–209, June 2017. WOS:000400721500009.

[26] ZhiWei He, XinLiang Li, and Xian Liang. Nonlinear spectral-like schemes for hybrid schemes. *Science China Physics, Mechanics and Astronomy*, 57(4):753–763, April 2014.

[27] Xin-liang Li, Yan Leng, and Zhi-wei He. Optimized sixth-order monotonicity-preserving scheme by nonlinear spectral analysis: optimized monotonicity-preserving scheme. *International Journal for Numerical Methods in Fluids*, 73(6):560–577, October 2013.

[28] Sergio Pirozzoli. On the spectral properties of shock-capturing schemes. *Journal of Computational Physics*, 2006.

[29] V.A. Titarev and E.F. Toro. Finite-volume WENO schemes for three-dimensional conservation laws. *Journal of Computational Physics*, 201(1):238–260, November 2004.

[30] H.C Yee, N.D Sandham, and M.J Djomehri. Low-Dissipative High-Order Shock-Capturing Methods Using Characteristic-Based Filters. *Journal of Computational Physics*, 150(1):199–238, March 1999.

Declaration of interests

☒ The authors declare that they have no known competing financial interests or personal relationships that could have appeared to influence the work reported in this paper.

☐The authors declare the following financial interests/personal relationships which may be considered as potential competing interests:

CONFLICT OF INTEREST

☑ The Article I have submitted to the journal for review is original, has been written by the stated authors and has not been published elsewhere.

☑ The Images that I have submitted to the journal for review are original, was taken by the stated authors, and has not been published elsewhere.

☑ This manuscript has not been submitted to, nor is under review at, another journal or other publishing venue.

☑ The authors have no affiliation with any organization with a direct or indirect financial interest in the subject matter discussed in the manuscript

☐ The below authors have affiliations with organizations with direct or indirect financial interest in the subject matter discussed in the manuscript: